

Learning Efficient and Effective Trajectories for Differential Equation-based Image Restoration

Zhiyu Zhu, Jinhui Hou, Hui Liu, Huanqiang Zeng, and Junhui Hou, *Senior Member, IEEE*

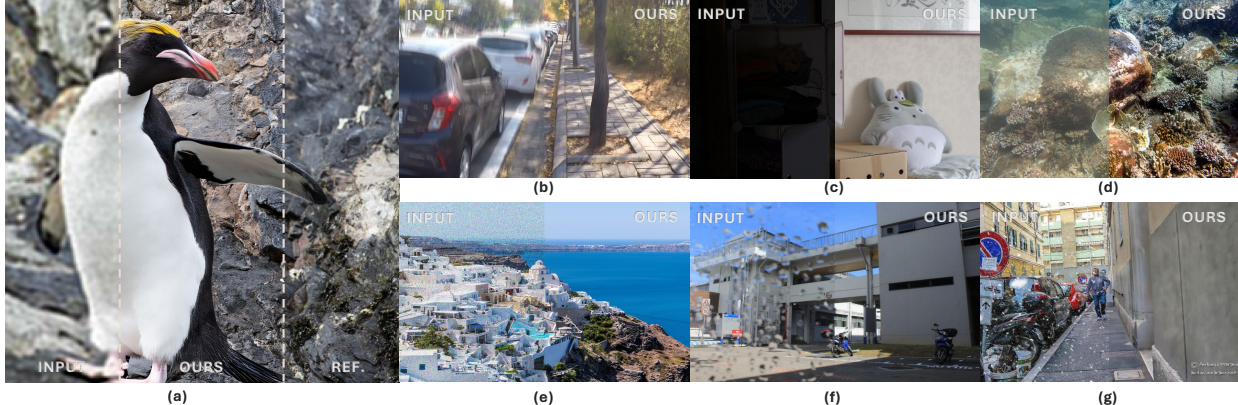


Fig. 1. Visual demonstration of the reconstruction performance of the proposed method across various image restoration tasks, where (a)-(e) witness its prowess in single image super-resolution, deblurring, low-light enhancement, underwater enhancement, denoising, raindrop removal, and desnowing, respectively. Impressively, benefiting from the strong capacity of diffusion models, the proposed method excels at producing content clearer than the **Reference** images in (a).

Abstract—The differential equation-based image restoration approach aims to establish learnable trajectories connecting high-quality images to a tractable distribution, e.g., low-quality images or a Gaussian distribution. In this paper, we reformulate the trajectory optimization of this kind of method, focusing on enhancing both reconstruction quality and efficiency. Initially, we navigate effective restoration paths through a reinforcement learning process, gradually steering potential trajectories toward the most precise options. Additionally, to mitigate the considerable computational burden associated with iterative sampling, we propose cost-aware trajectory distillation to streamline complex paths into several manageable steps with adaptable sizes. Moreover, we fine-tune a foundational diffusion model (FLUX) with 12B parameters by using our algorithms, producing a unified framework for handling 7 kinds of image restoration tasks. Extensive experiments showcase the significant superiority of the proposed method, achieving a maximum PSNR improvement of 2.1 dB over state-of-the-art methods, while also greatly enhancing visual perceptual quality. Project page: <https://zhu-zhiyu.github.io/FLUX-IR/>.

Index Terms—Image Restoration, Diffusion Models, Reinforcement Learning.

This work was supported in part by the NSFC Excellent Young Scientists Fund 62422118, in part by the Hong Kong Research Grants Council under Grant 11218121, and in part by Hong Kong Innovation and Technology Fund ITS/164/23. Zhiyu Zhu and Jinhui Hou contributed to this paper equally. (*Corresponding author: Junhui Hou*).

Zhiyu Zhu, Jinhui Hou, and Junhui Hou are with the Department of Computer Science, City University of Hong Kong, Hong Kong SAR (e-mail: zhiyuzhu2@my.cityu.edu.hk; jhhou3-c@my.cityu.edu.hk; jh.hou@cityu.edu.hk).

Hui Liu is with the School of Computing and Information Sciences, Saint Francis University, Hong Kong SAR (e-mail: h2liu@sfsu.edu.hk).

Huanqiang Zeng is with the School of Engineering, Huaqiao University, Quanzhou 362021, China, and also with the School of Information Science and Engineering, Huaqiao University, Xiamen 361021, China (e-mail: zeng0043@hqu.edu.cn).

I. INTRODUCTION

IMAGE restoration involves the enhancement of low-quality images affected by various degradations such as underwater and low-light conditions, raindrops, low-resolution, and noise to achieve high-quality outputs. It serves as a fundamental processing unit for visual recognition [1], [2], communication [3] and virtual reality [4]. Traditional image restoration methods typically rely on optimization procedures incorporating human priors such as sparsity, low rankness, and self-similarity [5], [6]. The emergence of deep learning techniques [7] has significantly transformed this domain. Initially delving into neural network architectures [8], image restoration has progressed beyond simple regression networks [8]–[11], exploring avenues like adversarial training [12], [13], algorithm unrolling [14]–[16] and flow-based methods [17]–[19].

Recently, a new category of generative models, namely diffusion models, has shown their strong potential for image synthesis and restoration [20], [21]. Generally, diffusion models construct probabilistic flow (PF) between a tractable distribution and the target distribution. The forward process typically involves incrementally introducing noise until reaching a manageable distribution, often a Gaussian. On the other hand, the reverse process can be obtained by maximizing the posterior of the forward Markov chain [22] or by sampling the reverse stochastic differential equation (SDE) [23], [24] or ordinary differential equation (ODE) [24].

Three categories of methods stand out for harnessing the potent generative capabilities of diffusion models for image restoration. The first category [25]–[27] leverages the progressive integration nature of the differential equations to maximize the diffusion posterior on the scene of a low-quality image, then progressively reversing to the high-quality

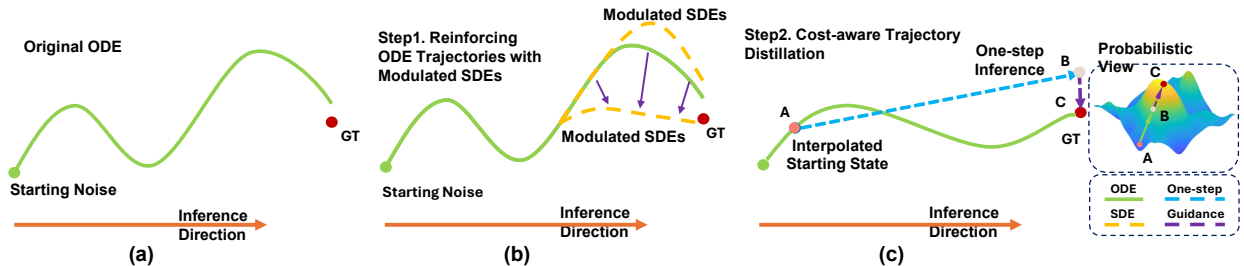


Fig. 2. Illustration of the workflow of the proposed method. Given a pre-trained diffusion model for image restoration, our trajectory optimization process contains the following two stages. (1) **Reinforcing ODE Trajectories with Modulated SDEs** in (b), which aligns the deterministic ODE trajectory shown in (a) to the most effective modulated SDE trajectory. (2) **Cost-aware trajectory distillation** in (c), which achieves high-quality one-step inference via delicate designs based on the task, with the knowledge of the original pre-trained model preserved. Note that to preserve the original knowledge of the pre-trained diffusion model, we aim to find a trajectory with less modification of gradient $\frac{dX}{dt}$. Through theoretical analyses and experimental validations, we find that for image restoration tasks, degraded measurements usually lie in the low probability region from the probabilistic space of high-quality samples. Thus, we also utilize the input measurements as negative guidance to rectify the gradient of log-density. As shown in the sub-figure of the probabilistic view, A, B, and C correspond to the low-quality measurement, reconstructed sample, and reconstruction by a low-quality image as negative guidance, respectively. We refer the readers to Fig. 8, which illustrates the trajectories directly from the diffusion data points.

samples. Although sampling-based methods can directly take advantage of large, pre-trained models and get rid of network training, the posterior optimization process may take more time and computational resources [25], [28], and their performance is noncompetitive compared with supervised training diffusion model [29]. The second category incorporates the reconstruction outcomes from a fixed pre-trained diffusion model as a prior [30], subsequently refining these outcomes through trainable neural networks, akin to algorithm unrolling techniques. Lastly, the third set of methods [20], [29] trains a diffusion trajectory conditioned on low-quality samples [29] or establishes a direct linkage between low-quality and high-quality image distributions [31]. Since the diffusion trajectory is explicitly refined by training on the paired dataset, this kind of approach has the most potential and effectiveness.

Due to the probabilistic nature and separate training approach of diffusion models, the reverse generation trajectory might exhibit instability or chaos [32]. To tackle such an issue, some work tends to rectify the generation trajectories to be straight [32] or directly train a consistency model [33]. Although this manner allows us to achieve adversarial training during the diffusion process, excessive regularization could significantly impair diffusion performance. As shown in Fig. 2, we aim to re-align the diffusion trajectory towards the most effective path using a reinforcement learning approach. Furthermore, considering that the resulting trajectories may be complex and require extensive steps for sampling, we then propose a novel trajectory distillation process to alleviate this issue, which analyzes and lessens the cost of a diffusion model distillation process. Extensive experiments demonstrate the significant advantages of the proposed trajectory augmentation strategies on various image restoration tasks over state-of-the-art methods.

In summary, we make the following key contributions in this paper:

- we propose a novel trajectory optimization paradigm for boosting both the efficiency and effectiveness of differential equation-based image restoration methods;
- we theoretically examine the accumulated score estimation error in diffusion models for image restoration and introduce a reinforcement learning-based ODE trajectory augmentation algorithm that leverages the modulated

SDE to generate potential high-quality trajectories;

- we improve the inference efficiency by introducing an acceleration distillation process, where we preserve the model's original capacity via investigating the distillation cost and utilizing the low-quality images for initial state interpolation and diffusion guidance;
- we establish new records on various image restoration tasks, including de-raining, low-light, under-water enhancement, image super-resolution, image de-blurring, and image de-noising;
- we calibrate a unified diffusion model for various image restoration tasks, based on the recent foundational diffusion model named *FLUX-DEV* with 12B parameters.

The remainder of this paper is organized as follows. Sec. II briefly reviews related work concerning diffusion models. Additionally, Sec. III offers essential mathematical formulations serving as the foundational backdrop for the proposed approach. Sec. IV details the proposed method, followed by comprehensive experiments in Sec. V. Finally, Sec. VI concludes this paper.

II. RELATED WORK

The differential equation-based deep generative model [24] represents a kind of learning strategy inspired by physical non-equilibrium diffusion processes [34]. It involves a forward diffusion process that progressively introduces noise into the data until a tractable distribution is reached, followed by a reversal to establish the data generation process. Ho *et al.* [22] firstly explored an effective diffusion formulation by parameterizing the reverse process as maximizing the posterior of reverse steps. Song *et al.* [24], [35]–[37] generalized such discrete diffusion steps into a continuous formulation by stochastic differential equation. Thus, the diffusion process can then be treated as an integral of the corresponding differential equation. Besides, the ordinary differential equation introduced in [36] removes the additional noise in the reverse process, which enables more inference acceleration designs [38]–[40]. Xu *et al.* [41] introduced a Poisson noise-based diffusion model. Robin *et al.* [42] converted the diffusion process into the latent domain to achieve high fidelity high-resolution diffusion. Blattmann *et al.* [43], [44] extended the image

diffusion model into a high-dimensional video diffusion process. Karras *et al.* [45] examined different formulations of the diffusion model and proposed a concise formulation. Dockhorn *et al.* [46] augmented the diffusion space by introducing an auxiliary velocity variable and constructing a diffusion process running in the joint space. Chen *et al.* [47] conducted theoretical convergence analysis on the score-based diffusion model.

In addition to the above, some diffusion-based methods bridge the distributions between different types of images. For example, Liu *et al.* [48] constructed a diffusion bridge by applying maximum likelihood estimation of latent trajectories with input from an auxiliary distribution. Li *et al.* [49] proposed an image-to-image translation diffusion model based on a Brownian Bridge diffusion process. Zhou *et al.* [50] utilized the h -transform to make a constraint of the endpoint of forward diffusion with formulations of reverse process derived by reformulating Kolmogorov equations.

A. Sampling Strategies for Accelerating Diffusion Process

Given the progressive noise reduction process, hundreds of steps are usually required to sample high-quality images. One solution to expedite inference involves crafting a refined sampling strategy. For example, Song *et al.* [51] pioneered the use of denoising diffusion implicit models (DDIM) to hasten diffusion sampling by disentangling each step in a non-Markov Chain fashion. Leveraging the semi-linear attributes of ODE and SDE formulations in diffusion models, Lu *et al.* [38]–[40] introduced a series of integral solvers with analytic solutions for the associated ODEs or SDEs. Zhang *et al.* [52] delved into the significant variance in distribution shifts and isolated an exponential variance component from the score estimation model, thereby mitigating discretization errors. Zhou *et al.* [53] introduced learnable solvers grounded in the mean value theorem for integrals. Xue *et al.* [54], [55] proposed accelerating diffusion sampling through an improved stochastic Adams method and precise ODE steps. Dockhorn *et al.* [56] advocated for higher-order denoising diffusion solvers based on truncated Taylor methods.

B. Trajectory Distillation-based Diffusion Acceleration

An alternative solution for accelerating generation involves directly adjusting diffusion trajectories. Liu *et al.* [32] introduced a method for straight flow regularization, which certifies the diffusion generation trajectory to be linear. Song *et al.* [33], [57] presented the consistency model, aligning each point on the trajectory directly with noise-free endpoints. Kim *et al.* [58] introduced trajectory consistency distillation to regularize gradients that can consistently map to corresponding points on the trajectory. Moreover, Zhou *et al.* [59], [60] proposed to make distillation of a pre-trained diffusion model to a student one-step generator via measuring discrepancy by additional learned score function.

Moving beyond training the diffusion model into a single-step generator, segmenting the process into multiple sections, with each being linear, presents a viable solution for rapidly generating high-quality outcomes in diffusion models [61]–[63].

C. Diffusion-based Image Restoration

In the realm of diffusion-based image restoration, we outline works that fall into two main categories: those employing a training-free diffusion sampling strategy [25]–[27], [64], [65] and those relying on model training [20], [29], [66]–[68].

Within the first category, Kawar *et al.* [25] introduced an unsupervised posterior sampling method for image restoration using a pre-trained diffusion model. Chung *et al.* [26] proposed to regularize the intermediate derivative from the reconstruction process to improve image restoration. Wang *et al.* [27] decoupled the image restoration into range-null spaces and focused on the reconstruction of null space, which contains the degraded information. Zhu *et al.* [64] combined the traditional plug-and-play image restoration method into the diffusion process. Regarding the training-based methods, Luo *et al.* [29] proposed a mean-reverting SDE with its reverse formulation to boost diffusion-based image restoration. Jiang *et al.* [69] proposed a wavelet-based diffusion model for low-light enhancement. Yi *et al.* [70] introduced a dual-branches diffusion framework combining reflectance and illumination reconstruction process. Wang *et al.* [71] proposed a DDIM-inspired diffusion-based framework for the distillation of an image restoration model. Tang *et al.* [72] introduced a transformer-based model for underwater enhancement using diffusion techniques. Recently, several works [68], [73]–[82] have focused on all-in-one image restoration using diffusion models. For example, TextPromptIR [77] and DA-CLIP [68] integrate textual or visual prompts to guide diffusion processes. Ai *et al.* [79] proposed a multimodal prompt learning method designed to leverage the generative priors of Stable Diffusion. Additionally, the Mixture-of-Experts (MoE) approach is adopted in MEASNet [81] and WM-MoE [83]. We also refer readers to [84] for the comprehensive survey on this topic.

Based on the aforementioned analysis for related work, although there are many works introducing the diffusion model to the field of image restoration, there is a limited number of works considering the accumulated score-estimation error by PF characteristics of the diffusion model. Moreover, acceleration of the sampling speed is also an essential research topic for differential equation-based image restoration frameworks.

III. PRELIMINARY

In this section, we provide a succinct overview of the diffusion model techniques, acceleration strategies (including trajectory solvers and distillation), and boosting strategies through alignment, laying the foundation for the subsequent sections.

A. Diffusion Model

Here, we consider image restoration as a case study to briefly elucidate the diffusion model.

Given a low-quality measurement denoted as $\mathbf{Y} \in \mathbb{R}^{H \times W \times 3}$, image restoration methods strive to reconstruct corresponding high-quality outputs, represented as $\mathbf{X} \in \mathbb{R}^{H' \times W' \times 3}$. The probabilistic nature of this restoration process involves maximizing a posterior $p_\theta(\mathbf{X}|\mathbf{Y})$, where θ the parameter set of the learnable neural

module. The differential equation-based methods [25] generally learn to construct a probabilistic flow (PF), e.g., $P(\mathbf{X}_0|\mathbf{X}_1, \mathbf{Y}), P(\mathbf{X}_1|\mathbf{X}_2, \mathbf{Y}), \dots, P(\mathbf{X}_{N-1}|\mathbf{X}_N, \mathbf{Y})$, to bridge the marginal distributions $P(\mathbf{X}_0)$ (same as $P(\mathbf{X})$) and $P(\mathbf{X}_N)$, usually as $\mathcal{N}(\mathbf{0}, \sigma_N^2 \mathbf{I})$ with σ being the standard deviation of noise.

In particular, the formulation based on DDPM [21], [22] constructs the PF connecting $P(\mathbf{X})$ and a standard Gaussian distribution $\mathcal{N}(\mathbf{0}, \mathbf{I})$, where the forward process is formulated as a diffusion process gradually substituting the data component with Gaussian noise, expressed as $\mathbf{X}_t = \bar{\alpha}_t \mathbf{X}_0 + \sqrt{(1 - \bar{\alpha}_t^2)} \epsilon_t$, $\epsilon_t \sim \mathcal{N}(\mathbf{0}, \mathbf{I})$. Conversely, the reverse process is deduced by computing the posterior $P(\mathbf{X}_t|\mathbf{X}_{t+1}, \mathbf{X}_0) = \frac{P(\mathbf{X}_{t+1}|\mathbf{X}_t)P(\mathbf{X}_t|\mathbf{X}_0)}{P(\mathbf{X}_{t+1}|\mathbf{X}_0)}$ with its resolution derived through the following ancestral sampling process:

$$\mathbf{X}_t \sim \mathcal{N}\left(\frac{1}{\sqrt{\alpha_{t+1}}}\left(\mathbf{X}_{t+1} - \frac{1 - \alpha_{t+1}}{\sqrt{1 - \bar{\alpha}_{t+1}}} \epsilon_{t+1}\right), \frac{1 - \bar{\alpha}_t}{1 - \bar{\alpha}_{t+1}}(1 - \alpha_{t+1}) \mathbf{I}\right). \quad (1)$$

As the noise component ϵ_{t+1} is typically challenging to handle, it is represented by a neural network parameterization $\epsilon_\theta(\mathbf{X}_{t+1}, t+1)$, trained using a loss term $\mathcal{L}_{DDPM} = \|\epsilon - \epsilon_\theta(\bar{\alpha}_t \mathbf{X}_0 + \sqrt{(1 - \bar{\alpha}_t^2)} \epsilon_t)\|_2^2$. By iteratively sampling Eq. (1), we can deduce \mathbf{X}_0 from the sample \mathbf{X}_N of a tractable distribution. Essentially, these sampling procedures serve to connect samples from two distributions along a high-dimensional trajectory, when minimizing the step size from the discrete to continuous spaces, i.e., $\Delta \bar{\alpha} \rightarrow d\alpha$.

Score-based models [24] achieve diffusion model generalization by reformulating the forward process via the following SDE:

$$d\mathbf{X} = f(\mathbf{X}, t)dt + g(t)d\omega, \quad (2)$$

where $t \in [\delta, T]$ denotes the timestamp of the diffusion process, with δ serving as a small number for numerical stability. The reverse SDE can be expressed as

$$d^{(s)}\mathbf{X} = [f(\mathbf{X}, t) - g^2(t)\nabla_x \log P(\mathbf{X})]dt + g(t)d\omega. \quad (3)$$

Furthermore, by redefining Kolmogorov's forward equation [24], an equivalent reverse ODE formulation emerges:

$$d^{(o)}\mathbf{X} = \left[f(\mathbf{X}, t) - \frac{1}{2}g^2(t)\nabla_x \log P(\mathbf{X})\right]dt. \quad (4)$$

Based on the diffusion strategies for $f(\mathbf{X}, t)$ and $g^2(t)$, the score-based diffusion models can be categorized into two variants, namely *variance preserving* (VP) or *variance exploding* (VE). Specifically, VP entails $f(\mathbf{X}, t) = \frac{d \log \alpha_t}{dt} \mathbf{X}$ and $g^2(t) = \frac{d\sigma_t^2}{dt} - 2\frac{d \log \alpha_t}{dt} \sigma_t^2$, where $\sigma_t = \sqrt{1 - \alpha_t^2}$, while VE involves $f(\mathbf{X}, t) = \mathbf{0}$ and $g^2(t) = \frac{d\sigma_t^2}{dt}$.

B. Integral Solver

To derive the reconstruction sample, we can calculate the integral of the reverse ODE trajectory in Eq. (4) as $\hat{\mathbf{X}}_0 = \mathbf{X}_T + \int_T^0 [f(\mathbf{X}, t) - \frac{1}{2}g^2(t)\nabla_x \log P(\mathbf{X})]dt$. Given the deterministic nature of the entire process, an analytical formulation can be leveraged. For the first time, DPM-Solver [38], [39]

introduces an exact solution based on the semi-linear property of the diffusion model, expressed as

$$\mathbf{X}_{t-\Delta t} = \frac{\alpha_{t-\Delta t}}{\alpha_t} \mathbf{X}_t - \alpha_{t-\Delta t} \int_{\lambda_t}^{\lambda_{t-\Delta t}} e^{-\lambda} \hat{\epsilon}_\theta(\hat{\mathbf{X}}_\tau, \tau) d\lambda, \quad (5)$$

where λ denotes the log-SNR (Signal-to-Noise Ratio), i.e., $\lambda := \log(\frac{\alpha_t}{\sigma_t})$. By computing this integral using various Order Taylor series for the non-linear term $\hat{\epsilon}_\theta(\hat{\mathbf{X}}_\lambda, \lambda)$, we can finally derive the result.

C. Rectified Flow & Trajectory Distillation

As a kind of naturally easily sampled model, the rectified flow-based method learns a straight flow between the random noise and target image domain, whose forward and reverse generation differential equations are identical, formulated as

$$d^{(o)}\mathbf{X}_t = (\mathbf{X}_0 - \mathbf{X}_T)dt. \quad (6)$$

It parameterizes a neural network to directly learn the slope $\mathbf{X}_0 - \mathbf{X}_T$ from \mathbf{X}_t . Similarly, distillation-based enhancement [33], [85] of diffusion models aims to regularize the inherent trajectory pattern to derive the diffusion models, which can be easily sampled. The nature of such kind of methods is to regularize

$$\mathcal{L}_{slope} = \mathcal{D}(\mathcal{C}(\mathbf{X}_t, t, \theta), \mathcal{C}(\mathbf{X}_s, s, \phi)), \quad (7)$$

where $\mathcal{C}(\cdot)$ denotes a consistency model or the ODE/SDE integrator, solving the integral with outputting $\hat{\mathbf{X}}_0$ from an arbitrary intermediate state \mathbf{X}_s (resp. \mathbf{X}_t) with timestamp s (resp. t); θ (resp. ϕ) represents the model weights of the student (resp. teacher) network; ϕ can be exponential moving average between the student net and original pre-trained model; and $\mathcal{D}(\cdot, \cdot)$ indicates the divergence metric for two inputs, such as L1/L2 norm and LPIPS [86].

D. Reinforcement Tuning of Diffusion Models

Given that the diffusion model is trained using discrete trajectory points, the accrued errors during the inference process are typically overlooked. Promising solutions to address these issues are found in reinforcement learning-based methods [87], [88], which optimize entire trajectories in a decoupled fashion. Specifically, these methods begin by constructing diffusion trajectories using the reverse SDE formulation of the diffusion model. The quality of the generated samples is then assessed using a reward model. The approach further enhances the probability of high-quality trajectories by aligning the trajectory expectations toward the high-quality points.

IV. PROPOSED METHOD

A. Overview

Learning effective and efficient trajectories is critical for differential equation-based image restoration. Due to the inherent Markov Chain property of the diffusion model, which leads to an interdependent iterative generation process, optimizing the entire trajectory requires the simultaneous optimization of multiple timestamps, i.e., networks, making it both time- and resource-consuming, and potentially intractable. In this work,

we propose a reinforcement learning-inspired alignment process in Sec. IV-B for improving restoration ability. Specifically, by projecting the accumulated error back to different steps, we theoretically reason the necessity of adaptively modulating the noise intensity of differential equations. Based on that, we align the ODE trajectory with the most effective alternative drawn from multiple candidate trajectories that are sampled by solving different modulated SDEs.

Subsequently, in Sec. IV-C, we propose a cost-aware trajectory distillation strategy to improve efficiency. This strategy capitalizes on the intrinsic properties of generative models and image restoration tasks to alleviate the burden of distillation. Given that low-quality samples typically reside in the low-probability regions of the target high-quality distribution, we guide the distillation trajectory in the opposite direction using the provided low-quality samples. Furthermore, since low-quality samples correspond to the same scene as their high-quality counterparts, we initiate the generation process from an interpolated state by the given low-quality sample, rather than the pure noise. Note that the proposed strategy can be adapted to both score-based [24] and rectified flow-based [32] diffusion models. Due to page limits, we mainly utilize the formulation of a score-based diffusion model in this paper, and we also refer readers to the *Supplementary Material* for extensive theoretical elaborations.

B. Reinforcing ODE Trajectories with Modulated SDEs

Diffusion models are usually trained through individual steps originating from the decoupled PF. However, during the inference phase, they usually operate in a progressively noise-removing manner. Due to inherent score function errors, these models often accumulate inaccuracies. While optimizing the entire trajectory could mitigate this issue, traditional diffusion models, even with ODE-solvers, struggle to yield satisfactory outcomes within a limited number of steps. Differently, we propose to align the learned trajectories with the most effective alternatives through reinforcement learning. Generally, our reinforcement learning-inspired approach [89], [90] aims to maximize the expectation of a reward function as

$$\nabla_{\theta} \mathcal{L} = -\nabla_{\theta} \mathbb{E}_{x \sim P_{\theta}(\mathbf{X})} \mathcal{R}(\mathbf{X}), \quad (8)$$

where $\mathcal{R}(\cdot)$ measures the quality of the sample \mathbf{X} ; $P_{\theta}(\mathbf{X})$ illustrates the distribution of \mathbf{X} conditioned on parameter θ . Given the deterministic nature of ODE sampling, optimizing the ODE towards the optimal trajectory could lead to maximizing the likelihood of obtaining the optimal sample ($P_{\theta}(\mathbf{X}_{optimal}) \rightarrow 1$). Unfortunately, the deterministic property of ODE trajectory also makes it difficult to generate diverse trajectories given a randomly initialized starting noise point. It cannot meet the reinforcement learning needs, which requires diverse alternatives to measure and select a better optimization direction. Thus, we argue that a *potential solution* for reinforcement training-based ODE trajectory augmentation should involve leveraging SDE to produce diverse restoration trajectories and aligning the deterministic ODE trajectory with the most effective SDE trajectory. However, the SDE is formulated with a fixed noise intensity level, which is too rigid

and inflexible to adapt to different conditions. As theoretically proven in Sec. I of the *Supplementary Material*, for an image restoration trajectory ended with \mathbf{X}_0 , we need to adjust the intensity of injected noise, conditioned on the reconstruction error $\|\mathbf{X}_0 - \mathbf{X}_0^*\|_2$ and corresponding timestamp t , where \mathbf{X}_0^* represents the ground-truth high-quality samples. Thus, a more flexible and controllable SDE formulation is necessary to reinforce the ODE trajectory.

Building upon above analyses, we utilize *modulated SDE* (M-SDE), dynamically adjusted by a non-negative factor learned from $\|\mathbf{X}_0 - \mathbf{X}_0^*\|_2$ and timestamp t through a small MLP parameterized with ψ , denoted as $\gamma_{\psi} (\|\mathbf{X}_0 - \mathbf{X}_0^*\|_2, t) > 0$. Serving as a versatile sampling trajectory, M-SDE encompasses ODE, SDE, and DDIM-like sampling, each tailored through distinct parameterizations [52], [91]. In what follows, we give the detailed formulations of M-SDE with score-based and rectified flow-based diffusion models.

1) *Score-based Diffusion*: The inverse M-SDE of the diffusion forward process, as described in Eq. (2), can be explicitly formulated as

$$d^{(\gamma)} \mathbf{X} = \left[f(x, t) - \frac{1 + \gamma_{\psi}^2}{2} g^2(\mathbf{X}, t) \nabla_x \log p(\mathbf{X} | \mathbf{Y}) \right] dt \quad (9)$$

$$+ \gamma_{\psi} g(\mathbf{X}, t) d\hat{\omega}.$$

Moreover, the integral solvers for the VP-M-SDE and VE-M-SDE can be respectively written as

$$\mathbf{X}_{t-\Delta t} = \frac{\alpha_{t-\Delta t}}{\alpha_t} \mathbf{X}_t - (1 + \gamma_{\psi}^2) \epsilon_{\theta} \left(\frac{\alpha_{t-\Delta t}}{\alpha_t} \sigma_t - \sigma_{t-\Delta t} \right) \quad (10)$$

$$- \sqrt{2} \gamma_{\psi} \epsilon \alpha_{t-\Delta t} \sqrt{\log \frac{\alpha_{t-\Delta t}}{\alpha_t}},$$

$$\mathbf{X}_{t-\Delta t} = \mathbf{X}_t - (1 + \gamma_{\psi}^2) \epsilon_{\theta} (\sigma_t - \sigma_{t-\Delta t}) \quad (11)$$

$$- \sqrt{2} \gamma_{\psi} \epsilon \sqrt{\sigma_t^2 - \sigma_{t-\Delta t}^2}.$$

We refer readers to Sec. II of the *Supplementary Material* for the proof.

2) *Rectified Flow-based Diffusion*: The following M-SDE formulation has the same PF as the ODE formulation of the rectified flow-based model in Eq. (6):

$$d^{(\gamma)} \mathbf{X} = \mathbf{X}_0 dt + \frac{t - \gamma}{1 - t} \mathbf{X}_T dt + \sqrt{2(\gamma - 1)} d\omega. \quad (12)$$

Moreover, the integration formula of Eq. (12) can be formulated as

$$\mathbf{X}_{t-\Delta t} = \frac{[\mathbf{X}_t - \alpha_t \Delta_t \frac{d\mathbf{X}_t}{dt} - \beta_k \epsilon]}{(1 + \alpha_t \Delta_t - t) + \sqrt{(t - \alpha_t \Delta_t)^2 + \beta_k^2}}, \quad (13)$$

where α_t is a scalar ($\alpha_t > 1$) and

$$\beta_k = \sqrt{\frac{(t - \Delta_t)^2 [1 - (t - \alpha \Delta_t)]^2}{[1 - (t - \Delta_t)]^2} - (t - \alpha \Delta_t)^2}. \quad (14)$$

We refer readers to Sec. III of the *Supplementary Material* for the detailed proof.

With the M-SDE formulation derived, we adopt the following loss to align the ODE trajectory to that of the “Best-of- N ” M-SDE at each step:

$$\mathcal{L}_A(t_i) = \mathcal{D}(\mathbf{X}_{t_i}^{(o)}, \mathbf{X}_{n^*, t_i}), \quad (15)$$

where $\mathbf{X}_{t_i}^{(o)} = \Psi_{t_i}^\tau(d^{(o)}\mathbf{X}, \mathbf{X}_\tau)$ denotes a noised state on the reverse ODE trajectory with timestamp t_i ; $\mathbf{X}_{n^*, t_i} = \Psi_{t_i}^\tau(d^{(\gamma)}\mathbf{X}, \mathbf{X}_\tau)$ is the corresponding noised state from the “Best-of- N ” reverse M-SDE trajectory; $\Psi_{t_i}^\tau(\cdot, \cdot)$ denotes the integration from timestamp τ to t_i through a typical integral solver (e.g., Eqs. (5), (10), (11), or (13)) with the reverse process formulation of the differential equation (i.e., Eqs. (4), (6), (9), or (12)) and the initial state as the first and second inputs.

Algorithm 1 summarizes the entire optimization process. Through such a reinforcement learning process, the proposed method can even be trained with some non-differentiable metrics, e.g., NIQE. We refer readers to Sec. V-B (resp. V-C) for the detailed settings of the reward and divergence measurements in task-specific (resp. unified) experiments.

Notably, by integrating the reinforcement learning strategy, our method dynamically approximates the ODE trajectories through adaptively sampled high-performance M-SDE trajectories, diverging from conventional reliance on static or predefined solutions. This shift can effectively mitigate overfitting and over-regularization constraints inherent to rigid optimization frameworks, thereby enhancing model generalization capabilities through stochastic trajectory sampling and iterative optimization refinement.

C. Distillation Cost-aware Diffusion Sampling Acceleration

In this section, we first explicitly model the cost-value of the diffusion model distillation process. Then, based on both empirical and theoretical results of distillation cost, we propose a novel trajectory distillation pipeline to manage high-quality few-step inference, which consists of a multi-step distillation strategy and a negative guidance policy from low-quality images.

Distillation Cost Analysis. To accelerate diffusion sampling, model distillation [32], [33], [92] condenses the knowledge from precise and multi-step sampling outcomes into shorter procedures, like the direct regularization in Eq. (7). However, this condensed distillation process may require adjustments to the initial neural parameter distributions, potentially decreasing network performance. To derive efficient and effective reconstruction, we argue that a good distillation training method for diffusion models should not only enable precise integration with fewer inference steps but also leverage the original Neuron-ODEs while minimizing alterations to neural network parameters. To this end, we propose a distillation cost-aware diffusion acceleration strategy that leverages the special characteristics of image restoration tasks to lessen the learning burden of the diffusion network.

Specifically, to quantify the extent of neural network adjustments, we introduce the trajectory distillation cost defined as

$$\mathcal{C} = \sum_{i=1}^k \left\| \tilde{\epsilon} \left(\frac{\mathbf{X}_i^{(i-1)}}{|t|_i^{i-1}} \middle| \frac{d\mathbf{X}_\epsilon}{dt} \right) - \epsilon_\theta(\mathbf{X}_{t_i}, t_i) \right\|_2, \quad (16)$$

Algorithm 1: Reinforcing ODE Trajectories with M-SDEs

```

Input : diffusion model parameter  $\theta$ , dataset distribution  $P(\mathbf{X}_0)$ , the number of SDE candidates  $N$ , and diffusion integrator  $\Psi(\cdot, \cdot)$ .
Output : Updated parameter  $\theta$ .
1 while not converged do
2   Sampling  $\mathbf{X}_0^* \sim P(\mathbf{X}_0)$ 
3    $\tau \leftarrow \text{Rand}(1, 2, \dots, T)$ 
4    $\mathbf{X}_T \sim \mathcal{N}(0, \mathbf{I})$ ;
5   if Score-based diffusion then
6     // Calculate noisy states on the reverse ODE trajectory via Eqs. (4) and (5)
7      $\mathbf{X}_\tau \leftarrow \Psi_T^\tau(d^{(o)}\mathbf{X}, \mathbf{X}_T)$ ;
8      $\{\mathbf{X}_{t_i}^{(o)}\} \leftarrow \{\Psi_{t_i}^\tau(d^{(o)}\mathbf{X}, \mathbf{X}_\tau), t_i \in [0, \tau]\}$ ;
9     // Generate states on the reverse M-SDE trajectories using Eqs. (9) and (10) (or (11))
10    for  $n = 1: N$  do
11       $\{\mathbf{X}_{n, t_i}\} \leftarrow \{\Psi_{t_i, n}^\tau(d^{(\gamma)}\mathbf{X}, \mathbf{X}_\tau), t_i \in [0, \tau]\}$ ;
12
13  else if Rectified Flow then
14    // Calculate the noisy states on the reverse ODE trajectory via Eq. (6)
15     $\mathbf{X}_\tau \leftarrow \Psi_\tau^\tau(d^{(o)}\mathbf{X}, \mathbf{X}_T)$ ;
16     $\{\mathbf{X}_{t_i}^{(o)}\} \leftarrow \{\Psi_{t_i}^\tau(d^{(o)}\mathbf{X}, \mathbf{X}_\tau), t_i \in [0, \tau]\}$ ;
17    // Generate noisy state candidates on the reverse M-SDE trajectory using Eqs. (12) and (13)
18    for  $n = 1: N$  do
19       $\{\mathbf{X}_{n, t_i}\} \leftarrow \{\Psi_{t_i, n}^\tau(d^{(\gamma)}\mathbf{X}, \mathbf{X}_\tau), t_i \in [0, \tau]\}$ ;
20
21  // Select the best trajectory via the reward process in reinforcement learning
22   $n^* \leftarrow \arg \max_{n \in [0, N]} \mathcal{R}(\mathbf{X}_{n, 0})$ ;
23  // Model update based on the loss in Eq. (15)
24   $\theta \leftarrow \theta + \alpha \nabla_\theta [\mathcal{D}(\mathbf{X}_{t_i}^{(o)}, \mathbf{X}_{n^*, t_i}) + \|\mathbf{X}_{t_i}^{(o)} - \mathbf{X}_0^*\|_2]$ 
Return:  $\theta$ .

```

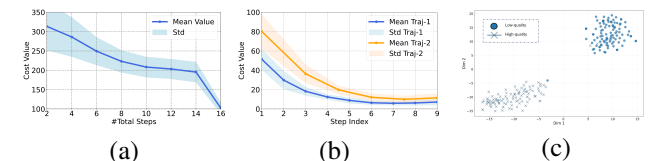


Fig. 3. Visualization of distillation costs and data distribution. (a) illustrates the *total distillation cost* (summation across steps) across trajectories with varying numbers of inference steps; (b) provides a detailed illustration of the *distillation cost for each step*. We first derive a dense trajectory with 40 timestamps between timestamp 0 to T . Subsequently, we implement two settings for few steps inference, utilizing step sizes of 5 and 8, resulting in the following timestamp-sparse trajectories, referred to as Traj-1 (8 steps) and Traj-2 (5 steps), respectively. Finally, we compute and visualize the distillation costs between the sparse and dense trajectories; and (c) illustrates the low-dimensional distribution of high-quality and low-quality images, revealing a clear distinction between the two data categories. This visualization highlights the divergent distribution patterns of high-quality and low-quality images. (Due to the page limits, we zoom out those figures.)

where k refers to the total number of steps in the student model, which is also known as the number of function evaluations (NFE), function $\tilde{\epsilon}(\mathbf{A}|\mathbf{B})$ denotes the inverse of $\epsilon(\cdot)$, calculating the corresponding ϵ value via making the \mathbf{B} term identical to the \mathbf{A} term, $\mathbf{X}_i^{(i-1)}$ symbols $\mathbf{X}_{i-1} - \mathbf{X}_i$. We refer readers to Sec. IV-A of the *Supplementary Material* for the detailed formulation process of $\tilde{\epsilon}$ and \mathcal{C} .

Algorithm 2: Diffusion Acceleration Distillation

Input : Diffusion model parameter θ , M-SDE $d^{(\gamma)}\mathbf{X}$, ODE $d^{(o)}\mathbf{X}$, dataset distribution $P(\mathbf{X}, \mathbf{Y})$.
Output : Updated parameter θ .

- 1 **while** not converged **do**
- 2 $\{\mathbf{X}_0^*, \mathbf{Y}\} \sim P(\mathbf{X}, \mathbf{Y})$ and $\epsilon \sim \mathcal{N}(0, \mathbf{I})$;
 // Initial state interpolation through Eq. (17)
- 3 $\mathbf{X}_{T-\delta} \leftarrow \alpha_{T-\delta} \mathbf{Y} + \sigma_{T-\delta} \epsilon$;
 // Sample generation with negative guidance of Eq. (19)
- 4 $\hat{\mathbf{X}}_0 \leftarrow \Psi_{T-\delta}^0(d^{(o)}\mathbf{X}, \mathbf{X}_{T-\delta})$;
 // Update via Eq. (18)
- 5 $\theta \leftarrow \theta - \nabla_\theta \mathcal{D}(\hat{\mathbf{X}}_0, \mathbf{X}_0^*)$.

Return: θ .

Algorithm 3: Inference Process of the Augmented Image Restoration Diffusion Models

Input : diffusion model $\epsilon_\theta(\cdot)$ or $v_\theta(\cdot)$, low quality sample \mathbf{Y} .
Output : Reconstruction $\hat{\mathbf{X}}_0$.

- 1 $\epsilon \sim \mathcal{N}(0, \mathbf{I})$
 // Interpolate the starting state via Eq. (17)
- 2 $\mathbf{X}_{T-\delta} \leftarrow \alpha_{T-\delta} \mathbf{Y} + \sigma_{T-\delta} \epsilon$;
- 3 **for** $t = T - \delta : 0$ **do**
- 4 // Derive the noise prediction with negative guidance of Eq. (19)
 $\hat{\epsilon}_\theta \leftarrow (1+w)\epsilon_\theta - w\tilde{\epsilon}$
 // Calculate the reverse integration via substituting $\hat{\epsilon}_\theta$ and \mathbf{X}_t into Eq. (5)
 $\mathbf{X}_{t-\Delta t} \leftarrow \Psi_{t-\Delta t}^t(d^{(o)}\mathbf{X}, \mathbf{X}_t)$;

Return: θ .

To investigate the characteristics of the distillation cost of the diffusion model, we calculate both the distillation cost of the whole trajectory and each step and visualize them in Fig. 3 (a) and (b). Moreover, we further visualize the distributions of low-quality and high-quality image via t-SNE in Fig. 3 (c). With acknowledgment of the aforementioned distillation-based prior, we can draw the following observations:

- the distillation cost exhibits a negative correlation with the total number of steps (Fig. 3(a));
- initial steps contribute significantly to the overall distillation cost (Fig. 3(b));
- the low-quality images lie in the distinctive distribution compared with the high-quality images, as illustrated in Fig. 3 (c).

The first observation supports the superiority of recent multi-step distillation models [58], [61], [93] over their single-step counterparts. Nonetheless, for efficient inference of the diffusion model, the inclusion of few or even single-step models remains essential. Furthermore, in Sec. IV of the *Supplementary Material*, we delve into the theoretical exploration of the existence of cost-effective multi-step distillations. Moreover, drawing on the second and third observations, we can outline the subsequent steps to alleviate the substantial learning burden associated with the distillation process.

1) *Interpolation of the Initial State*: Regarding the second observation, during the initial inference stages, diffusion models must synthesize data from pure noise—a challenging yet crucial aspect of the generation process. Considering

the inherent characteristics of the image restoration task, the available low-quality input inherently retains a higher fidelity to the structural and semantic content of the target high-quality reconstruction compared to stochastically sampled Gaussian noise. Consequently, it can be leveraged as a robust preliminary estimation to guide the iterative refinement process toward optimal restoration results. Thus, to alleviate this burden, we propose synthesizing the noised latent representation as

$$\mathbf{X}_{T-\delta} = \alpha_{T-\delta} \mathbf{Y} + \sigma_{T-\delta} \epsilon, \quad (17)$$

where $\delta \geq 0$ is chosen sufficiently small to ensure SNR ($\frac{\alpha_{T-\delta}}{\sigma_{T-\delta}}$) to be sufficiently small. Subsequently, we can train our acceleration distillation neural network via the following loss term:

$$\mathcal{L}_D = \mathcal{D}(\hat{\mathbf{X}}_0, \mathbf{X}^*), \quad (18)$$

where $\hat{\mathbf{X}}_0 = \Psi_0^{T-\delta}(d^{(o)}\mathbf{X}, \mathbf{X}_{T-\delta})$ represents reverse integration result from timestamp $T - \delta$ to 0, and \mathbf{X}^* indicates the reference high-quality images. Furthermore, we theoretically analyze this noised latent interpolation method in Sec. V of *Supplementary Material*.

2) *Low-quality Images as Sampling Guidance*: In the realm of image restoration, our objective is to reconstruct a high-quality image \mathbf{X} from a low-quality measurement \mathbf{Y} . Moreover, based on the previous observation, we propose leveraging low-quality images as sampling guidance, which can amplify the positive restoration components from the diffusion model, to ease the learning burden of the diffusion model. From a probabilistic perspective, the training of diffusion-based image restoration models strives to improve the alignment of final reconstruction \mathbf{X}_0 with reference image \mathbf{X} under the given condition \mathbf{Y} , i.e., improving $\mathbf{P}(\mathbf{X}_0 = \mathbf{X} | \mathbf{Y})$. Let $\mathbf{Y} = \mathcal{H}(\mathbf{X})$ with $\mathcal{H}(\cdot)$ being the degradation function. Considering that the degradation Jacobian matrix $\frac{\partial \mathcal{H}(\mathbf{X})}{\partial \mathbf{X}}$ often deviates from the identity matrix, there exists a notable discrepancy between the $\mathbf{P}(\mathbf{X}_0)$ and $\mathbf{P}(\mathbf{Y}_0)$. To address this, we propose a parameterized score function guided by the following principles:

$$\hat{\epsilon}_\theta = (1+w)\epsilon_\theta - w\tilde{\epsilon}, \quad (19)$$

where w denotes a scalar for guidance strength, and $\tilde{\epsilon}$ indicates predicted noise by maximizing the posterior likelihood on low-quality images, serving as guidance for the diffusion process, which can be calculated by inverting the integral process:

$$\tilde{\epsilon} = \frac{\frac{\alpha_0}{\alpha_t} \mathbf{X}_t - \mathbf{Y}}{\sqrt{1-\alpha_t^2} \alpha_0 - \sqrt{1-\alpha_0^2}}. \quad (20)$$

Algs. 2 and 3 summarize the training and inference process in detail, respectively.

Remark. During the distillation phase, we harness the intrinsic characteristics of the image restoration task to mitigate the substantial challenges associated with few-step inference. Specifically, we implement interpolation of the initial state and negative guided sampling to address two critical issues: the significant estimation errors encountered during the high-noise initial stage and the complexities associated with modeling the probabilistic data space. These features distinguish our approach from existing techniques. Besides, our framework

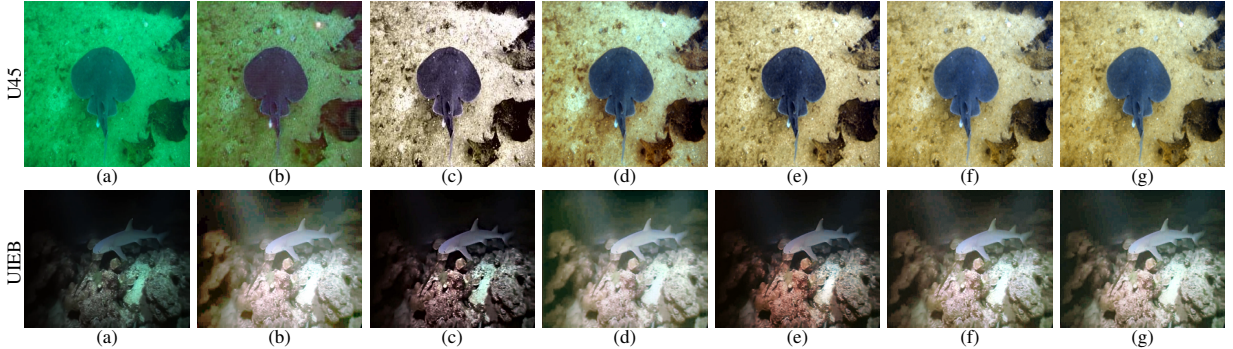


Fig. 4. Visual comparison of underwater image enhancement on U45 [94] and UIEB [95] datasets. U45 (**top**): (a) low-quality input, (b) CycleGAN [96], (c) MLLE [97], (d) HCLR [98], (e) SemiUIR [99], (f) Ours($NFE = 1$) and (g) Ours($NFE = 10$). UIEB (**bottom**): except (b) reference image, the remaining columns are the same as those of U45. More visual results can be found in the *Supplementary Material*.

TABLE I

QUANTITATIVE COMPARISONS OF DIFFERENT METHODS ON UNDERWATER ENHANCEMENT. THE BEST AND SECOND-BEST RESULTS ARE HIGHLIGHTED IN **BOLD** AND UNDERLINE, RESPECTIVELY. “ \uparrow ” (RESP. “ \downarrow ”) MEANS THE LARGER (RESP. SMALLER), THE BETTER. “NFE” DENOTES THE NUMBER OF FUNCTION EVALUATIONS, WHICH CAN BE INTERPRETED AS THE INFERENCE STEPS. \ddagger INDICATES RESULTS FROM THE FIRST STAGE: REINFORCING ODE TRAJECTORIES WITH MODULATED SDES.

Method	$ _{NFE} $	UIEBD				C60				U45			
		PSNR \uparrow	SSIM \uparrow	UCIQE \uparrow	UIQM \uparrow	UCIQE \uparrow	UIQM \uparrow	UCIQE \uparrow	UIQM \uparrow	PSNR \uparrow	SSIM \uparrow	UCIQE \uparrow	UIQM \uparrow
Water-Net [95] TIP'19	1	16.31	0.797	0.606	2.857	<u>0.597</u>	2.382	0.599	2.993				
Ucolor [100] TIP'21	1	21.09	0.872	0.580	3.048	0.553	2.482	0.573	3.159				
MLLE [97] TIP'22	1	19.56	0.845	0.588	2.646	0.569	2.208	0.595	2.485				
NAFNet [101] ECCV'22	1	22.69	0.870	0.592	3.044	0.559	2.751	0.594	3.087				
Restormer [10] CVPR'22	1	23.70	0.907	0.599	3.015	0.570	2.688	0.600	3.097				
SemiUIR [99] CVPR'23	1	24.31	0.901	0.605	3.032	0.583	2.663	0.606	3.185				
HCLR-net [98] IJCV'24	1	25.00	0.925	0.607	3.033	0.587	2.695	0.610	3.103				
Ours\ddagger	10	25.08	0.913	0.615	3.142	0.571	3.663	0.612	4.282				
Ours	2	26.29	<u>0.935</u>	<u>0.624</u>	3.112	<u>0.610</u>	4.004	<u>0.636</u>	4.527				
Ours	1	26.25	0.938	<u>0.623</u>	3.135	0.582	<u>3.814</u>	0.617	4.413				

TABLE II

QUANTITATIVE COMPARISON OF RECENT STATE-OF-THE-ART METHODS ON UNDERWATER ENHANCEMENT USING NO-REFERENCE METRICS AND COMPUTATIONAL EFFICIENCY ANALYSIS. \ddagger INDICATES RESULTS FROM THE FIRST STAGE: REINFORCING ODE TRAJECTORIES WITH MODULATED SDES.

Method		C60				Complexity		
		MUSIQ \uparrow	CLIPQA \uparrow	MANIQA \uparrow	NIQE \downarrow	Param (M)	TFLOPs	Runtime (s)
SemiUIR [99] CVPR'23	41.768	0.256	0.191	5.379	1.65	0.210	0.13	
HCLR-net [98] IJCV'24	<u>45.524</u>	0.331	0.221	<u>4.834</u>	19.55	2.099	0.18	
Ours\ddagger (NFE=10)	45.514	<u>0.350</u>	<u>0.220</u>	5.055	68.03	1.305	3.17	
Ours (NFE=2)	47.019	0.458	<u>0.293</u>	4.271	68.03	1.305	0.65	
Ours (NFE=1)	44.583	0.337	0.205	4.926	68.03	1.305	0.31	

aims to improve the overall efficiency and effectiveness of inference processes in complex environments, thereby paving the way for future research and applications.

V. EXPERIMENTS

In this section, we thoroughly evaluate the proposed trajectory optimization strategies across various image restoration tasks. Initially, we confirm the task-specific enhancement capabilities by training individual smaller networks for tasks such as de-raining, low-light enhancement, and underwater enhancement in Sec. V-B. Furthermore, in Sec. V-C, we produce a unified perceptual image restoration network by fine-tuning the state-of-the-art T2I foundational diffusion framework *FLUX-DEV* [117], which has 12B parameters.

TABLE III

QUANTITATIVE COMPARISONS OF DIFFERENT METHODS ON LOW-LIGHT ENHANCEMENT. THE BEST AND SECOND-BEST RESULTS ARE HIGHLIGHTED IN **BOLD** AND UNDERLINE, RESPECTIVELY. “ \uparrow ” (RESP. “ \downarrow ”) MEANS THE LARGER (RESP. SMALLER), THE BETTER. “NFE” DENOTES THE NUMBER OF FUNCTION EVALUATIONS, WHICH CAN BE INTERPRETED AS THE INFERENCE STEPS. \ddagger INDICATES RESULTS FROM THE FIRST STAGE: REINFORCING ODE TRAJECTORIES WITH MODULATED SDES.

Method		LOL				LOL-v2			
		NFE	PSNR \uparrow	SSIM \uparrow	LPIPS \downarrow	NFE	PSNR \uparrow	SSIM \uparrow	LPIPS \downarrow
Zero-DCE [107] CVPR'20	1	14.861	0.562	0.335	1	18.059	0.580	0.313	
EnlightenGAN [108] TIP'21	1	17.483	0.652	0.322	1	18.640	0.677	0.309	
RetinexNet [109] BMVC'18	1	16.770	0.462	0.474	1	18.371	0.723	0.365	
DRBN [110] CVPR'20	1	19.860	0.834	0.155	1	20.130	0.830	0.147	
KimD [111] MM'19	1	20.870	0.799	0.207	1	17.544	0.669	0.375	
KimD++ [112] IJCV'20	1	21.300	0.823	0.175	1	19.087	0.817	0.180	
MIRNet [113] TPAMI'22	1	24.140	0.842	0.131	1	20.357	0.782	0.317	
LLFlow [103] AAAI'22	1	25.132	0.872	0.117	1	26.200	0.888	0.137	
Retinexformer [104] ICCV'23	1	27.180	0.850	-	1	27.710	0.856	-	
PyDiff [114] IJCAI'23	4	27.090	0.879	0.100	-	-	-	-	
LLFormer [105] AAAI'23	1	25.758	0.823	0.167	1	26.197	0.819	0.209	
SNR-Aware [106] CVPR'22	1	26.716	0.851	0.152	1	27.209	0.871	0.157	
LLFlow-L-SKF++ [115] TPAMI'24	1	26.894	0.879	0.095	1	28.453	0.909	0.117	
GSAD [116] NeurIPS'23	20	27.839	0.877	0.091	10	28.818	0.895	0.095	
Ours\ddagger	10	28.581	0.883	0.084	10	29.535	0.898	0.086	
Ours	2	28.360	<u>0.886</u>	0.088	2	29.956	<u>0.905</u>	<u>0.089</u>	
Ours	1	28.184	0.885	0.086	1	29.911	0.904	0.101	

A. Experimental Settings

1) Datasets: We employ multiple commonly used benchmark datasets to conduct experiments under two scenarios.

Task-specific restoration. We conducted three task-specific restoration tasks, including underwater image enhancement, low-light image enhancement, and image deraining. The dataset details are provided as follows:

- Underwater Enhancement.** The UIEB dataset [95] consists of 950 real-world underwater images and includes two subsets: 890 raw underwater images with the corresponding high-quality reference images and 60 unpaired challenging underwater images (labeled as C60). We randomly sampled 800 image pairs for training, and 90 image pairs for testing. We further utilize the unpaired dataset, i.e., C60 and U45 [118], for real-world underwater image enhancement testing.
- Low-light Enhancement.** LOLv1 [109] contains 485 low/normal-light image pairs for training and 15 pairs for testing, captured at various exposure times from the real scene. LOLv2 [119] is split into two subsets: LOLv2-real and LOLv2-synthetic. In this work, we utilize the LOLv2-real, which comprises 689 pairs of low-/normal-light images for training and 100 pairs for testing, collected by adjusting the exposure time and ISO.

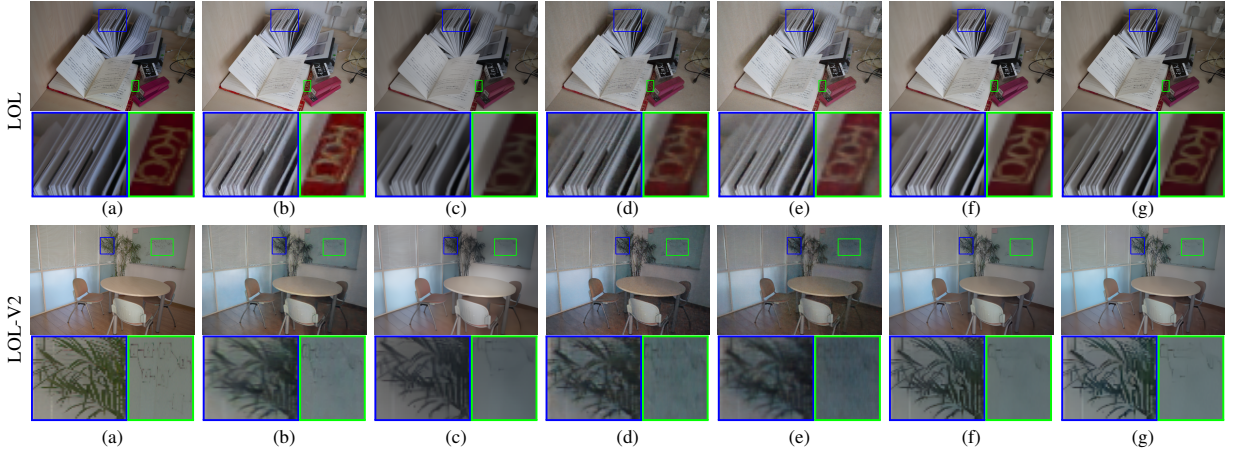


Fig. 5. Visual comparison of low-light enhancement on LOL and LOLV2 datasets. **LOL (top)**: (a) reference images, (b) CID [102], (c) CLIPFlow [103], (d) RetinexFormer [104], (e) LLFormer [105], (f) Ours ($NFE = 1$), (g) Ours ($NFE = 10$). **LOL-V2 (bottom)**: except (b) SNR-Aware [106], the remaining columns are the same as those of LOL. Below each figure, we also visualize zoom-in regions marked by the blue and green boxes. More visual results can be found in the *Supplementary Material*.

TABLE IV

QUANTITATIVE COMPARISON OF RECENT STATE-OF-THE-ART METHODS ON LOW-LIGHT ENHANCEMENT USING NO-REFERENCE METRICS AND COMPUTATIONAL EFFICIENCY ANALYSIS. THE BEST AND SECOND-BEST RESULTS ARE HIGHLIGHTED IN **BOLD** AND UNDERLINE, RESPECTIVELY. \ddagger INDICATES RESULTS FROM THE FIRST STAGE: REINFORCING ODE TRAJECTORIES WITH MODULATED SDEs.

Method	LOL				LOL-v2				Complexity		
	MUSIQ↑	CLIPQA↑	MANIQA↑	NIQE↓	MUSIQ↑	CLIPQA↑	MANIQA↑	NIQE↓	Param (M)	FLOPs (T)	Runtime (s)
LLFlow [103] AAAI'22	73.212	0.380	0.560	5.672	71.001	0.428	0.590	5.566	37.68	1.05	0.58
SNR-Aware [106] CVPR'22	65.228	0.254	0.334	5.177	62.507	0.306	0.334	4.622	39.13	0.10	0.02
LLFormer [105] AAAI'23	60.760	0.331	0.314	3.582	52.127	0.291	0.265	4.379	24.55	0.22	0.74
GSAD [116] NeurIPS'23	73.555	0.458	0.559	5.805	<u>71.721</u>	<u>0.552</u>	<u>0.595</u>	5.150	17.36	0.27	0.86
LLFlow-L-SKF++ [115] TPAMI'24	73.874	0.422	0.575	5.549	70.851	0.384	0.568	5.590	39.77	1.10	0.75
Ours[†] (NFE=10)	74.407	0.530	0.604	5.246	72.586	0.528	0.637	5.269	17.36	0.27	0.81
Ours (NFE=2)	<u>73.976</u>	0.503	0.563	5.047	70.578	<u>0.557</u>	0.565	4.962	17.36	0.27	0.15
Ours (NFE=1)	73.966	0.570	0.569	4.817	71.633	0.538	0.592	4.961	17.36	0.27	0.06

- **Image De-raining.** We utilize several datasets for this task, including Raindrop [120], Outdoor-Rain [121], Rain100L/H [122], Rain200L/H [122], DID-Data [123], and DDN-Data [124]. Specifically, Raindrop contains 861 images for training and 58 images for testing. Outdoor-Rain consists of 8,250 and 750 images for training and testing, respectively. Rain100L/H and Rain200L/H include 1,800 images for training, with 100 images and 200 images for testing, respectively. DID-Data has 12,000 images for training and 1,200 images for testing. DDN-Data comprises 12,600 and 1,400 image pairs for training and testing, respectively.

Unified restoration. We collect images for 7 kinds of image restoration tasks. The details of these datasets are listed below:

- **Image Super-Resolution.** The training dataset consists of 3,450 high-quality 2K images collected from DIV2K [125] and Flickr2K [126]. We utilize the Real-ESRGAN [127] degradation pipeline to generate LQ-HQ training pairs. The testing set contains 100 images from DIV2K-Val [125].
- **Image Desnowing.** The Snow100K-L [128] dataset includes 100k synthesized snowy images with corresponding snow-free reference images and snow masks. We randomly selected 1,872 (resp. 601) images forming the

training (resp. testing) dataset for image de-snowing.

- **Image Deblurring.** The GoPro [129] dataset contains 3,214 blurred images with a size of 1280×720 . The images are divided into 2,103 training images and 1,111 test images. The dataset consists of pairs of a realistic blurry image and the corresponding ground truth sharp images that are obtained by a high-speed camera.

- **Image Denoising.** The noisy images were derived by randomly corrupting the aforementioned high-quality SR datasets with Gaussian noise by a standard deviation of 50. We further utilize BSD500 [130] and SIDD [131] for generalization ability testing.

- **Low-light Enhancement.** We employ LOLv1 [109] for fine-tuning and test.

- **Image De-raining.** Raindrop [120] and Outdoor-rain [121] datasets are utilized.

- **Underwater Enhancement.** The UIEB dataset [95] is employed.

2) **Methods under comparison & Evaluation metrics:** On the experiments of specific image restoration tasks, we compared the proposed method with the state-of-the-art methods in the fields of underwater enhancement, low-light enhancement, and deraining. For unified image restoration, we mainly compared the proposed method with the unified method for fairness. Moreover, according to the ill-posed nature of the

image restoration inverse problems and to preserve the strong image synthesis capacity of the pre-trained FLUX model, we did not enforce the proposed method to fully approach the reference image and utilized more unpaired and perceptual scores, e.g., NIQE [132], MUSIQ [133], and CLIPQA [134], to validate the performance of our FLUX-IR.

B. Task-Specific Image Restoration Diffusion Models

Implementation Details. For task-specific image restoration, e.g., underwater enhancement, low-light enhancement, and deraining, we trained a diffusion model for each particular degradation. Specifically, by using the proposed algorithm, we trained three separate diffusion networks based on GSAD [116] for low-light enhancement, de-raining, and underwater enhancement tasks. During this process, we utilized PSNR (resp. MSE) as the reward (resp. divergence measurement) for the ODE alignment step, respectively. The model was trained on an RTX 3090 for 30,000 iterations for both alignment and acceleration, employing the Adam optimizer with a learning rate of $5e^{-5}$, a training patch size of 256×256 , and a batch size of 2.

Underwater Image Enhancement. The quantitative comparisons are presented in Table I, demonstrating that the proposed method significantly outperforms state-of-the-art techniques, such as HCLR-net [98] and SemiUIR [99], on the UIEBD dataset by **1.3 dB**. The single step model even beats the multi-step counterparts. We visualized the enhanced results in Fig. 4. For the U45 dataset, due to the fact that there is no ground truth available, we only provided the low-quality input with the corresponding reconstruction. Our method reconstructs more clear details with visually pleasing color, especially for the 1st and 3rd rows on the U45 dataset. Moreover, on the UIEB dataset, our method may even generate more visually pleasing results than the reference image, shown as the first example. The enhanced image has more soft light, making it easier to distinguish the foreground object, e.g., the shark, and the background scene, e.g., coral. Additionally, quantitative evaluation on the C60 is provided in Table II, where our proposed method achieves substantial improvements over recent state-of-the-art methods across multiple no-reference metrics. Specifically, our two-step model (NFE=2) achieves the highest MUSIQ, CLIPQA, and MANIQA scores, alongside the lowest NIQE, clearly surpassing SemiUIR [99] and HCLR-net [98]. Notably, our method also demonstrates competitive computational efficiency, balancing runtime and performance effectively.

Low-light Image Enhancement. Table III presents the performance of various methods in low-light enhancement. It is important to note that *LOL-V1* serves as a highly competitive benchmark. Nonetheless, the proposed method demonstrates a notable improvement of **0.7 dB**. Furthermore, it achieves an enhancement exceeding **1.1 dB** on *LOL-v2*. Table IV reveals the proposed method achieves competitive results across multiple no-reference metrics, such as the highest MUSIQ and MANIQA scores on both LOL and LOL-v2, indicating high perceptual quality. In terms of complexity,

the proposed method with NFE=1 demonstrates remarkable efficiency, requiring only **0.06** seconds, which is significantly faster than other methods, e.g., LLFormer [105] and LLFlow-L-SKFF++ [115]. Fig. 5 visually compares the results of different methods. The proposed method generates more clear details than other compared methods, e.g., the leaves in the 1st and 3rd examples from the LOL-v2 dataset, and the small word "ano" in 3rd examples marked by the green rectangle. Moreover, even for the region with extremely low-light conditions, our method can also accurately reconstruct it, shown as the local zoom in the region with green rectangle in the first example of the LOL dataset.

Deraining. Substantial improvements of **2.1 dB** and **0.9 dB** are evidenced in Tables V and VI, respectively. Notably, the proposed method, employing both dual-step and single-step approaches, demonstrates superior performance compared to specialized deraining diffusion models. This underscores the necessity and effectiveness of our strategies for ODE trajectory augmentation and simplification. Furthermore, Table VIII reveals that our proposed method achieves superior perceptual scores, such as MUSIQ and CLIPQA, while exhibiting favorable computational efficiency. Fig. 6 provides visual results of different methods. Specifically, for the task of raindrop removal, we visualized the regions seriously deteriorated by raindrops, e.g., the roof of a car and shelves on the playground, in zoom-in sub-figures, where the input measurement, i.e., Fig. 6-(a), indicates the object structure has been greatly damaged. However, even with this kind of degradation, the proposed method can accurately reconstruct the original structure, validating the superiority of the proposed method. The first sample of the Raindrop dataset also validates that the proposed method can correct the color of texture since the other methods show more red components compared with the proposed method. Meanwhile, we also visualize the deraining experimental results of *Outdoor-Rain* dataset in Fig. 6. Note that our method is not specifically trained to reconstruct words. However, to our surprise, the strong restoration capacity of the proposed method enables accurate reconstruction of words and numbers, e.g., "2.8" in the first sample and "U" in the second sample of the *Outdoor-Rain* dataset.

Table VII further presents comprehensive comparisons with state-of-the-art methods on more challenging deraining datasets, including Rain100L/H [122], Rain200L/H [122], DID-Data [123], and DDN-Data [124]. Our method exhibits consistent superiority, achieving the highest PSNR and SSIM scores across most datasets. While the performance on Rain200L and Rain200H datasets appears moderate compared to some recent methods, our approach still demonstrates substantial improvements over the baseline diffusion model GSAD, with notable gains of **+1.06 dB** on Rain200L and **+1.89 dB** on Rain200H. These improvements highlight the effectiveness of our method in handling complex rainy scenarios, even when faced with more challenging datasets.

Based on the aforementioned analysis, we conclude that the proposed method can accurately reconstruct both natural texture and cultural markers, and greatly outperform the state-of-the-art method by a large extent, validating the effectiveness of the proposed image restoration diffusion augmentation

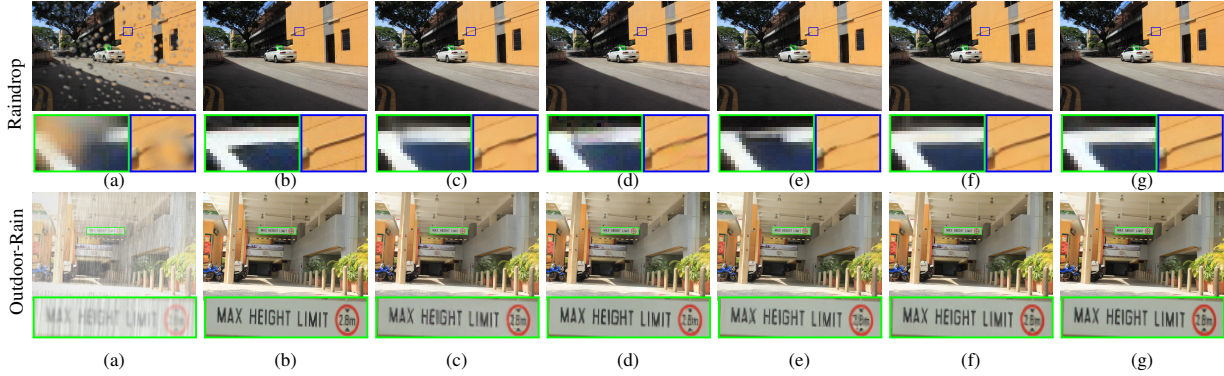


Fig. 6. Visual comparison on the tasks of raindrop removal and image deraining. Raindrop removal (**top**): (a) low-quality input, (b) reference samples, (c) IDT [135], (d) GridFormer [136], (e) RainDropDiff [65], (f) Ours ($NFE = 1$), (g) Ours ($NFE = 10$). Deraining (**bottom**): (a) low-quality input, (b) reference samples, (c) GridFormer [136], (d) WeatherDiff64 [65], (e) WeatherDiff128 [65], (f) Ours ($NFE = 1$), (g) Ours ($NFE = 10$). More visual results can be found in the *Supplementary Material*.

TABLE V

QUANTITATIVE COMPARISONS OF DIFFERENT METHODS ON IMAGE DERAINING. THE BEST AND SECOND-BEST RESULTS ARE HIGHLIGHTED IN **BOLD** AND UNDERLINED, RESPECTIVELY. “ \uparrow ” (RESP. “ \downarrow ”) MEANS THE LARGER (RESP. SMALLER), THE BETTER. “NFE” DENOTES THE NUMBER OF FUNCTION EVALUATIONS, WHICH CAN BE INTERPRETED AS THE INFERENCE STEPS. \ddagger INDICATES RESULTS FROM THE FIRST STAGE: REINFORCING ODE TRAJECTORIES WITH MODULATED SDES.

Method	NFE	Outdoor-Rain		
		PSNR \uparrow	SSIM \uparrow	LPIPS \downarrow
pix2pix [137] CVPR’17	1	19.09	0.7100	-
HRGAN [138] CVPR’19	1	21.56	0.8550	0.154
PCNet [139] TIP’21	1	26.19	0.9015	0.132
MPRNet [140] CVPR’21	1	28.03	0.9192	0.089
Restormer [10] CVPR’22	1	29.97	0.9215	0.074
WeatherDiff ₆₄ [65] TPAMI’23	25	29.41	0.9312	0.059
WeatherDiff ₁₂₈ [65] TPAMI’23	25	29.28	0.9216	0.061
DTPM [141] CVPR’24	50	30.48	0.9210	0.054
DTPM [141] CVPR’24	10	30.92	0.9320	0.062
DTPM [141] CVPR’24	4	30.99	0.9340	0.064
Ours\ddagger	10	32.08	<u>0.9424</u>	0.065
Ours	2	33.10	0.9439	<u>0.058</u>
Ours	1	<u>32.61</u>	0.9419	0.064

strategy.

C. Unified Perceptual Image Restoration with FLUX-IR

Implementation Details. We trained a single diffusion model to handle various types of degradation. Here, we constructed the unified image restoration network based on FLUX-DEV [117]. Specifically, we first trained a low-quality U-Net encoder to make its feature map consistent with those from high-quality images. Then, we further trained a Control-Net by XFLUX [152]. We began by training a low-quality U-Net encoder to ensure its feature map aligned with those from high-quality images. Subsequently, we trained a control network using XFLUX [152]. During this training, we integrated features from XFLUX and the pre-trained encoder into the DiT structure of FLUX to enable rapid adaptation of our FLUX-IR framework. The model was trained on five NVIDIA H800 GPUs for 20,000 iterations, utilizing the Adam optimizer, a learning rate of $5e^{-5}$, a training patch size of 1024^2 , and a batch size of 128 (with gradient accumulation). After this pre-training phase, we enhanced the FLUX-IR model using our proposed strategy. Given the significant size and training

TABLE VI

QUANTITATIVE COMPARISONS OF DIFFERENT METHODS ON RAINDROP REMOVING. THE BEST AND SECOND-BEST RESULTS ARE HIGHLIGHTED IN **BOLD** AND UNDERLINED, RESPECTIVELY. “ \uparrow ” (RESP. “ \downarrow ”) MEANS THE LARGER (RESP. SMALLER), THE BETTER. “NFE” DENOTES THE NUMBER OF FUNCTION EVALUATIONS, WHICH CAN BE INTERPRETED AS THE INFERENCE STEPS. \ddagger INDICATES RESULTS FROM THE FIRST STAGE: REINFORCING ODE TRAJECTORIES WITH MODULATED SDES.

Method	NFE	Raindrop		
		PSNR \uparrow	SSIM \uparrow	LPIPS \downarrow
DuRN [142] CVPR’19	1	31.24	0.9259	-
RaindropAtt [143] ICCV’19	1	31.44	0.9263	0.068
AttentiveGAN [120] CVPR’18	1	31.59	0.9170	0.055
IDT [135] TPAMI’22	1	31.87	0.9313	0.059
RainDropDiff ₆₄ [65] TPAMI’23	25	32.29	0.9422	0.058
RainDropDiff ₁₂₈ [65] TPAMI’23	25	32.43	0.9334	0.058
AST-B [144] CVPR’24	1	32.38	0.9350	0.066
DTPM [141] CVPR’24	50	31.44	0.9320	0.044
DTPM [141] CVPR’24	10	31.87	0.9370	0.048
DTPM [141] CVPR’24	4	32.72	0.9440	0.058
Ours\ddagger	10	33.32	0.9388	0.044
Ours	2	33.69	<u>0.9444</u>	<u>0.047</u>
Ours	1	<u>33.63</u>	0.9459	0.052

costs associated with FLUX, we combined reinforcement learning and distillation into a single training phase, setting the diffusion timestamp to 9 and interpolating the initial state using the low-quality latent. We then applied reinforcement learning with guidance to further improve performance over a few inference steps. During this phase, the reward was calculated as the average of the following metrics: LPIPS, NIQE, MUSIQ, and CLIPQA, with normalization factors of -1 , -20 , 70 , and 1 , respectively. During training, we sampled the data from the task of super-resolution at a frequency of $5/10$ and others are the same as $5/60$.

Experimental Results. We validated the effectiveness of the proposed trajectory augmentation techniques in the unified image restoration task, which contains 7 distinct image restoration tasks. Experimental results are shown in Table IX. Benefiting from strong capacity and our delicately designed learning scheme, FLUX-IR achieves extraordinary performance on the perceptual metrics, which even beats the task-specific methods, e.g., Stable SR [30] and PASD [145] from the task of super-resolution. We want to note that accurately quantifying the

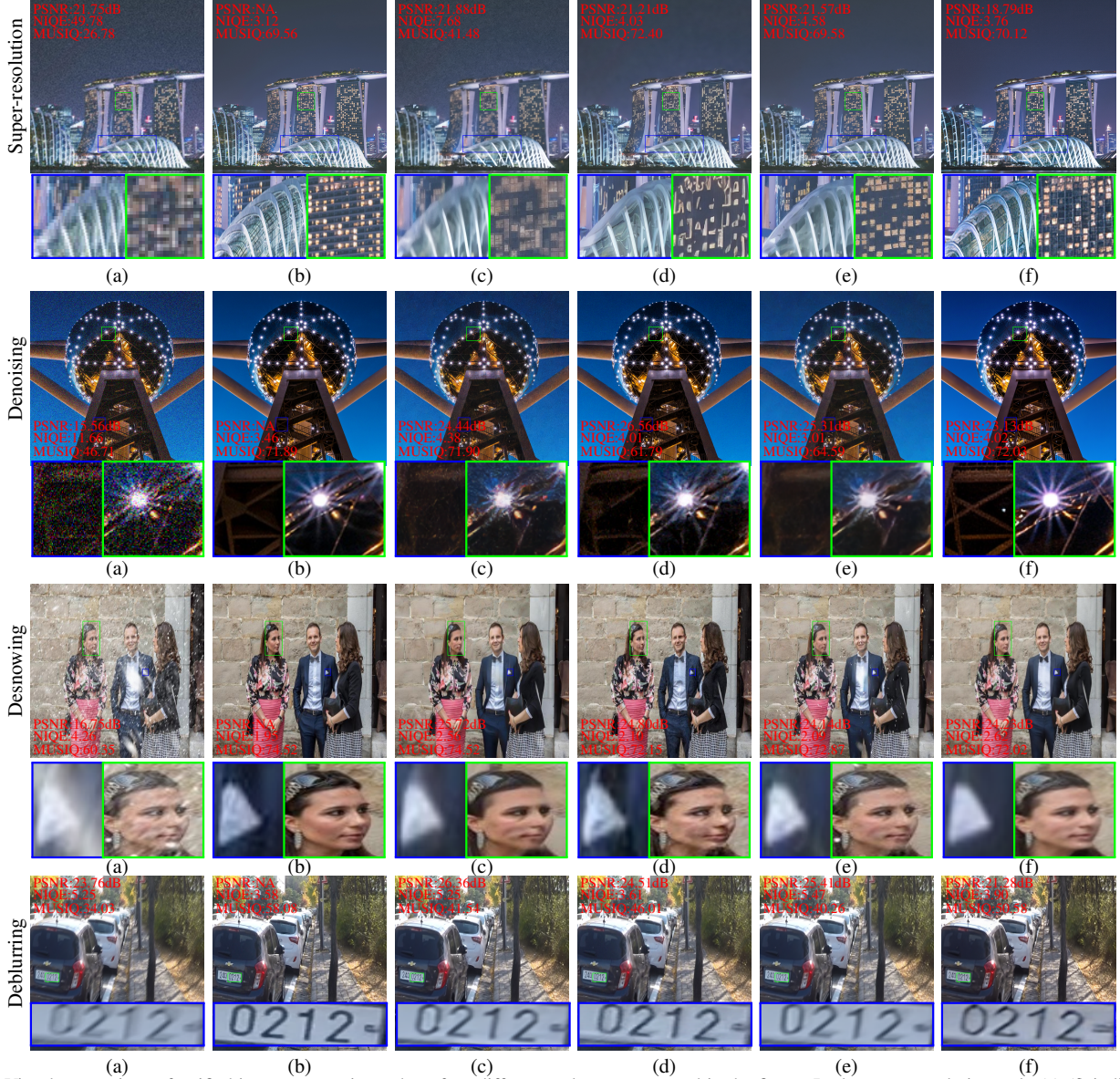


Fig. 7. Visual comparison of unified image restoration, where four different tasks are compared in the figure. In the super-resolution task, (a)-(f) indicates the input low-quality measurement, reference image, PASD [145], SeeSR [146], and FLUX-IR(Ours), respectively. For denoising, (c)-(e) represents AdaIR [76], DA-CLIP [68], and PromptIR [73], respectively. Moreover, for desnowing, (c)-(e) shows WGWS-Net [147], DA-CLIP [68], and DiffUIR [78], respectively. Finally for deblurring, (c)-(e) shows AdaIR [76], DA-CLIP [68], and DiffUIR [78], respectively. We annotated evaluation metrics of corresponding images by PSNR \uparrow , NIQE \downarrow , and MUSIQ \uparrow , respectively. More visual results can be found in the *Supplementary Material*.

perceptual performance is a difficult issue. The outstanding performance of the proposed method, which may generate more reasonable and clear structures even than reference images, may make evaluation more difficult.

We visually compare various methods in Fig. 7 across four tasks: super-resolution, denoising, deblurring, and desnowing, which were not previously illustrated. Corresponding metrics are annotated in the corners of the images. While reference-aware metrics such as PSNR are critical for traditional image restoration tasks, relying solely on these metrics is inadequate for assessing quality in real-world scenarios. For instance, in the super-resolution task, manual interpolation, as depicted in Fig. 7-SR-(a), achieves superior PSNR scores compared to all other methods, yet its visual quality is inferior. Furthermore, evaluating quality without reference poses significant chal-

lenges, and a single perceptual metric may exhibit instability under certain conditions. Therefore, our approach of integrating multiple perceptual metrics for reinforcement learning is both practical and effective.

The following is a detailed analysis of the visual comparison results. Specifically, for the task of *super-resolution*, FLUX-IR significantly outperforms the compared methods, particularly evident in the depiction of building details and the feathers of the parrot in the first and third rows, respectively. These results not only match but sometimes surpass the perceptual quality of the reference images. The strong capabilities of FLUX-IR are especially highlighted in human-related restoration, an area highly sensitive to our perception. As illustrated in the second row, FLUX-IR effectively generates realistic human faces and bodies, while the other methods struggle to produce

TABLE VII

QUANTITATIVE COMPARISON WITH STATE-OF-THE-ART TRANSFORMER-BASED AND DIFFUSION-BASED METHODS ON SIX DERAINING DATASETS. THE BEST AND SECOND-BEST RESULTS ARE HIGHLIGHTED IN **BOLD** AND UNDERLINED, RESPECTIVELY. \ddagger INDICATES RESULTS FROM THE FIRST STAGE: REINFORCING ODE TRAJECTORIES WITH MODULATED SDES.

Method	NFE	Rain100L		Rain100H		Rain200L		Rain200H		DID-Data		DDN-Data	
		PSNR↑	SSIM↑										
<i>Transformer-based:</i>													
Restormer [10] CVPR'22	1	38.99	0.9782	31.46	0.9042	40.99	0.9890	32.00	0.9329	35.29	0.9641	34.20	0.9571
IDT [135] TPAMI'22	1	41.59	0.9882	-	-	40.74	0.9884	32.10	<u>0.9344</u>	34.89	0.9623	33.84	0.9549
DRSformer [148] CVPR'23	1	42.50	0.9902	33.80	0.9372	41.23	0.9894	<u>32.17</u>	0.9326	35.35	0.9646	34.35	0.9588
FADformer [149] ECCV'24	1	42.92	0.9913	33.99	0.9394	41.80	0.9906	32.48	0.9359	<u>35.48</u>	<u>0.9657</u>	34.42	0.9602
<i>Diffusion-based:</i>													
DA-CLIP [68] ICLR'24	100	41.79	0.9863	33.91	0.9260	38.63	0.9772	28.53	0.8594	32.37	0.9126	32.16	0.9241
GSAD [116] NeurIPS'23	10	42.57	0.9903	34.19	0.9472	39.45	0.9851	28.60	0.9029	33.38	0.9431	34.34	0.9575
Ours\ddagger	10	43.77	0.9926	34.77	0.9544	40.44	0.9871	30.49	0.9217	35.37	0.9656	35.19	0.9655
Ours	2	44.38	0.9931	35.80	0.9562	40.51	0.9871	30.33	0.9181	35.50	0.9662	<u>35.16</u>	<u>0.9650</u>
Ours	1	<u>43.79</u>	0.9922	<u>35.30</u>	0.9518	40.29	0.9863	30.02	0.9145	35.22	0.9647	34.94	0.9631

TABLE VIII

QUANTITATIVE COMPARISON OF RECENT STATE-OF-THE-ART METHODS ON RAINDROP REMOVING USING NO-REFERENCE METRICS AND COMPUTATIONAL EFFICIENCY ANALYSIS. THE BEST AND SECOND-BEST RESULTS ARE HIGHLIGHTED IN **BOLD** AND UNDERLINED, RESPECTIVELY. \ddagger INDICATES RESULTS FROM THE FIRST STAGE: REINFORCING ODE TRAJECTORIES WITH MODULATED SDES

Method		Raindrop				Complexity		
		MUSIQ↑	CLIPQA↑	MANIQA↑	NIQE↓	Param (M)	FLOPs (T)	Runtime (s)
RainDropDiff ₁₂₈ [65] TPAMI'23		71.631	0.471	<u>0.501</u>	3.517	82.96	1.921	103.70
AST-B [144] CVPR'24		69.751	0.427	0.463	<u>3.272</u>	19.92	0.152	0.10
GridFormer [136] IJCV'24		69.829	<u>0.548</u>	0.486	3.684	30.20	1.010	0.87
Ours\ddagger (NFE=10)		70.464	0.555	0.472	3.710	68.03	1.067	1.52
Ours (NFE=2)		71.872	0.504	0.505	3.535	68.03	1.067	0.32
Ours (NFE=1)		71.365	0.475	0.488	3.545	68.03	1.067	0.13

plausible outcomes. Similar trends are observed in the tasks of denoising and desnowing. Lastly, for deblurring, this task differs from previous challenges involving noise, snowflakes, and downsampling, as the deblurring process merely mixes without compromising the original images. Consequently, all methods produce plausible images, as shown in the last row of Fig. 7.

Additionally, we conducted denoising evaluations on BSD500 [130] and SIDD [131] datasets to demonstrate the generalization ability of our proposed Flux-IR, where we directly tested on these datasets without training on the relevant training sets. As shown in Table X, our Flux-IR demonstrates superior perceptual quality with best NIQE, MUSIQ, and MANIQA scores, highlighting the strong generalization ability of the proposed Flux-IR.

D. Ablation Studies

Reconstruction Performance. We have applied the detailed ablation studies of each trajectory augmentation technique in Table XI. Specifically, for reinforcement learning-based ODE alignment (*RL*), it improves both single and multiple-step image restoration. Notably, models utilizing single-step alignment exhibit substantial improvements, such as an increase from 20.92 dB to 24.54 dB on the Raindrop dataset. This enhancement is attributed to the significant simplification of the trajectory post-alignment, which reduces integral estimation errors and benefits single-step inference. Conversely, few-step distillation (*DISTILL*) improves single-step performance but

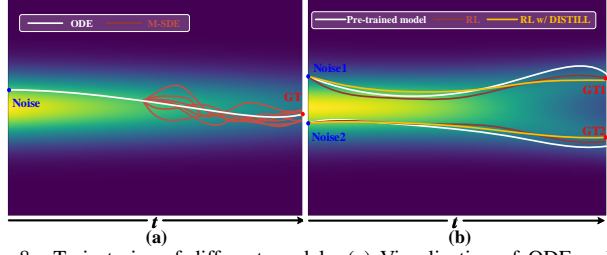


Fig. 8. Trajectories of different models. (a) Visualization of ODE and M-SDE trajectories for the pre-trained model. It can be seen that some M-SDE trajectories are more effective, being closer to the ground truth (GT) than the ODE counterpart. The optimal M-SDE trajectory is then selected as guidance for our reinforcement learning-based alignment process. (b) Visualization of ODE trajectories for the pre-trained model, our reinforced model, and our distilled model. “ t ” indicates the diffusion timestamp. Both reinforced and distilled models generate more effective ODE trajectories compared to the pre-trained model.

diminishes network performance with multiple steps. Furthermore, interpolation (*INTERP*) and guided sampling techniques (*NGS*) generally enhance single-step diffusion models by alleviating the burden on neural networks to directly match Gaussian noise distributions with real-world data. However, for multi-step diffusion models, the use of interpolated noisy latent and negative guidance from low-quality images may present limitations. We refer readers to the *Supplementary Material* for the visual demonstration.

Visualization of Trajectories. As our design is primarily centered on modeling trajectories of neural differential equations, we also analyze the variations in these trajectories to gain insights into the effects of our proposed method. As shown in Fig. 8-(a), we illustrate the ODE and M-SDE trajectories of the pre-trained model. The M-SDE trajectories exhibit more variance and potential compared to the ODE counterpart, which enables our reinforced ODE trajectory learning. Fig. 8-(b) depicts the ODE trajectories of the pre-trained, reinforced, and distilled models. Here, the reinforced ODE trajectory demonstrates a more direct path toward the target distribution, indicating that our reinforcement learning approach effectively optimizes the restoration path. Moreover, the distilled ODE trajectory closely approximates the reinforced trajectory, showcasing the efficacy of our trajectory distillation in preserving the optimized path while reducing computational complexity.

TABLE IX
QUANTITATIVE COMPARISONS OF DIFFERENT METHODS ON UNIFIED IR TASKS. “ \uparrow ” (RESP. “ \downarrow ”) MEANS THE LARGER (RESP. SMALLER), THE BETTER. \dagger MEANS THE COMPARED METHODS WERE DESIGNED AS UNIFIED IMAGE RESTORATION FRAMEWORKS.

Method	NFE	Super-resolution (DIV2K-Val [125])	Desnowing (Snow100K-L [128])	De-blurring (GoPro [129])	Denoising (DIV2K-Val [125])	Low-Light Enhancement (LOL [109])	Raindrop removal (Raindrop [120])	Deraining&Dehazing (Outdoor-rain [121])	Underwater Enhancement (UIEBD [95])
		NIQE \downarrow / MUSIQ \uparrow CLIPQA \uparrow / PSNR \uparrow	NIQE \downarrow / MUSIQ \uparrow CLIPQA \uparrow / PSNR \uparrow	NIQE \downarrow / MUSIQ \uparrow CLIPQA \uparrow / PSNR \uparrow	NIQE \downarrow / MUSIQ \uparrow CLIPQA \uparrow / PSNR \uparrow	NIQE \downarrow / MUSIQ \uparrow CLIPQA \uparrow / PSNR \uparrow	NIQE \downarrow / MUSIQ \uparrow CLIPQA \uparrow / PSNR \uparrow	NIQE \downarrow / MUSIQ \uparrow CLIPQA \uparrow / PSNR \uparrow	NIQE \downarrow / MUSIQ \uparrow CLIPQA \uparrow / PSNR \uparrow
SeeSR [146] CVPR’24	50	4.073 / 72.437 0.722 / 23.329	\times						
PASD [145] ECCV’24	20	3.676 / 71.738 0.695 / 23.143	\times						
DiffBIR \dagger [74] ECCV’24	50	4.333 / 64.672 0.651 / 22.548	\times						
DA-CLIP \dagger [68] ICLR’24	100	\times	2.775 / 69.394 0.375 / 28.641	3.937 / 39.925 0.212 / 28.619	5.091 / 58.098 0.584 / 26.979	5.208 / 70.500 0.633 / 26.768	4.817 / 67.592 0.488 / 31.207	\times	\times
DiffUIR \dagger [78] CVPR’24	3	\times	3.163 / 70.265 0.456 / 28.879	5.834 / 34.061 0.203 / 27.815	\times	4.904 / 71.389 0.378 / 25.269	\times	\times	\times
AdaIR \dagger [76] ICLR’25	1	\times	\times	5.514 / 33.263 0.198 / 28.464	4.458 / 59.714 0.611 / 25.953	4.713 / 70.859 0.404 / 22.409	\times	\times	\times
AutoDIR \dagger [75] ECCV’24	50	4.865 / 55.196 0.458 / 23.939	\times	6.164 / 33.354 0.197 / 28.444	5.095 / 58.399 0.515 / 28.081	4.200 / 71.095 0.398 / 22.896	3.365 / 68.723 0.403 / 32.332	\times	\times
WeatherDiff [65] TPAMI’23	25	\times	\times	\times	\times	\times	3.517 / 71.631 0.471 / 30.713	3.544 / 71.397 0.501 / 29.721	\times
AST-B [144] CVPR’24	1	\times	\times	\times	\times	\times	3.272 / 69.750 0.427 / 32.380	\times	\times
GridFormer [136] DCV’24	1	\times	2.918 / 70.854 0.488 / 30.792	\times	\times	\times	3.684 / 69.829 0.558 / 32.324	3.620 / 70.299 0.511 / 31.874	\times
WGWS-Net [147] CVPR’23	1	\times	3.345 / 70.167 0.507 / 28.933	\times	\times	\times	3.479 / 71.731 0.435 / 33.430	3.968 / 70.835 0.459 / 30.609	\times
NU ² Net [150] AAAI’23	1	\times	4.717 / 47.810 0.541 / 25.221						
HCLR-net [98] IICV’24	1	\times	4.803 / 48.623 0.593 / 24.998						
FLUX-IR (Ours)	20	3.491 / 73.188 0.721 / 20.248	2.769 / 65.985 0.440 / 23.442	4.578 / 46.728 0.233 / 23.884	3.631 / 72.657 0.685 / 24.531	4.045 / 73.233 0.484 / 25.029	3.201 / 70.105 0.507 / 25.846	2.804 / 70.631 0.514 / 24.734	4.515 / 49.867 0.574 / 23.275
FLUX-IR (Ours)	10	4.269 / 72.069 0.673 / 20.895	2.862 / 68.117 0.482 / 24.840	4.521 / 42.045 0.199 / 24.868	4.199 / 71.519 0.631 / 25.373	4.163 / 72.728 0.460 / 24.914	3.320 / 69.661 0.515 / 27.918	3.023 / 69.862 0.521 / 25.856	4.596 / 49.958 0.574 / 23.409

TABLE X

QUANTITATIVE COMPARISON OF THE GENERALIZATION ABILITY OF DIFFERENT UNIFIED IMAGE RESTORATION METHODS ON IMAGE DENOISING. NOTE THAT OUR TRAINING SET DOES NOT INCLUDE THE BSD500 AND SIDD DATASETS, WHERE SIDD IS A REAL-WORLD DENOISING DATASET. “ \uparrow ” (RESP. “ \downarrow ”) MEANS THE LARGER (RESP. SMALLER), THE BETTER.

Method	NFE	BSD500-Test [130]		SIDD [131]
		$\sigma = 30$	$\sigma = 50$	NIQE \downarrow / MUSIQ \uparrow CLIPQA \uparrow / MANIQ \uparrow
PromptIR [73] NeurIPS’23	1	10.724 / 29.481 0.701 / 26.214	12.797 / 37.948 0.782 / 22.211	5.143 / 44.790 0.449 / 0.307
AdaIR [76] ICLR’25	1	11.234 / 28.106 0.677 / 25.820	12.513 / 37.451 0.766 / 22.178	5.577 / 44.719 0.481 / 0.347
DA-CLIP [68] ICLR’24	100	10.972 / 29.167 0.340 / 25.729	9.893 / 27.994 0.485 / 23.819	8.197 / 43.735 0.383 / 0.240
AutoDIR [75] ECCV’24	50	5.866 / 47.230 0.452 / 33.065	4.959 / 46.304 0.513 / 31.670	9.414 / 42.997 0.351 / 0.295
FLUX-IR (Ours)	20	4.942 / 65.967 0.527 / 27.027	4.923 / 63.886 0.547 / 26.472	7.655 / 62.950 0.505 / 0.427
FLUX-IR (Ours)	10	5.826 / 60.572 0.447 / 28.521	5.894 / 58.529 0.482 / 27.021	7.686 / 58.661 0.431 / 0.366

Analysis of ODE Alignment with Modulated SDE. We investigated the effectiveness of aligning ODE with a modulated SDE (M-SDE) compared to direct ODE-SDE alignment. As shown in Table V-B, the M-SDE approach consistently performs better than direct SDE alignment across all evaluated datasets. This improvement holds whether using a learned γ or an optimally chosen fixed value, validating the effectiveness of our proposed alignment method. Furthermore, to better understand the role of the modulation parameter, we conducted an ablation study with various fixed γ values. Our experiments reveal that model performance is notably sensitive to the

TABLE XI
RESULTS OF THE ABLATIVE STUDY ON THE EFFECT OF THE PROPOSED TWO TRAINING AUGMENTATION TECHNIQUES. “RL” DENOTES THE REINFORCEMENT LEARNING-BASED ALIGNMENT. “DISTILL” REPRESENTS THE SINGLE-STEP DISTILLATION FOR INFERENCE ACCELERATION. “INTERP” INDICATES THE INTERPOLATION OF THE STARTING POINT. “NGS” REPRESENTS UTILIZING THE LOW-QUALITY IMAGE AS NEGATIVE GUIDANCE.

IDX.	RL	DISTILL	INTERP	NGS	NFE	UIEBD	Raindrop	LOL-v2						
						PSNR \uparrow SSIM \uparrow LPIPS \downarrow	PSNR \uparrow SSIM \uparrow LPIPS \downarrow	PSNR \uparrow SSIM \uparrow LPIPS \downarrow						
1	\times	\times	\times	\times	10	24.31 19.99	0.916 0.802	0.151 0.284	32.86 20.92	0.942 0.357	0.059 0.674	28.78 20.35	0.895 0.717	0.094 0.255
2	\checkmark	\times	\times	\times	10	25.08 21.06	0.913 0.715	0.162 0.457	33.32 24.54	0.938 0.807	0.044 0.266	29.54 21.35	0.898 0.690	0.086 0.263
3	\checkmark	\checkmark	\times	\times	10	24.04 25.80	0.856 0.923	0.225 0.153	30.26 33.93	0.920 0.942	0.057 0.049	28.19 29.75	0.863 0.904	0.137 0.096
4	\checkmark	\checkmark	\checkmark	\times	10	24.20 25.94	0.923 0.937	0.136 0.127	29.80 33.53	0.918 0.946	0.056 0.052	28.30 29.86	0.864 0.904	0.135 0.102
5	\checkmark	\checkmark	\checkmark	\checkmark	10	21.87 26.25	0.845 0.938	0.261 0.128	29.25 33.63	0.877 0.946	0.129 0.052	28.33 29.91	0.863 0.904	0.130 0.101

choice of γ , thus highlighting a key advantage of our learned γ approach, i.e., the model can automatically optimize its behavior for different datasets and degradation types by dynamically adapting the alignment during training, eliminating the need for manual parameter tuning while ensuring robust performance.

Different Distillation Schemes. We compared our approach against two state-of-the-art diffusion distillation methods: Consistency Model (CM) [33] and Consistency Trajectory Model (CTM) [151]. From Table XIII, it can be observed that the proposed distillation method yields consistent improvements across multiple datasets, highlighting its effectiveness in achieving efficient inference while ensuring high-quality

TABLE XII
RESULTS OF THE ABLATION STUDY ON PARAMETER γ OF THE PROPOSED MODULATED SDE.

	γ	UIEBD			Raindrop			LOL-v2		
		PSNR↑	SSIM↑	LPIPS↓	PSNR↑	SSIM↑	LPIPS↓	PSNR↑	SSIM↑	LPIPS↓
M-SDE	Learned γ	25.08	0.913	0.162	33.32	0.938	0.044	29.54	0.898	0.086
	0.05	24.84	0.911	0.165	33.21	0.944	0.053	29.37	0.902	0.097
	0.10	24.65	0.915	0.155	32.45	0.929	0.053	29.52	0.905	0.093
	0.15	24.48	0.917	0.159	30.09	0.831	0.150	29.51	0.889	0.087
	0.20	24.90	0.932	0.140	29.69	0.747	0.238	27.96	0.772	0.142
	0.25	24.32	0.922	0.145	29.35	0.744	0.243	27.18	0.708	0.152
	0.30	24.18	0.929	0.142	29.26	0.742	0.212	27.68	0.758	0.146
SDE ($\gamma = 1$)		24.52	0.928	0.147	32.18	0.939	0.065	29.23	0.895	0.097

TABLE XIII
RESULTS OF THE ABLATION STUDY ON DIFFERENT DISTILLATION SCHEMES. THE BEST RESULTS ARE HIGHLIGHTED IN **BOLD**.

Method	NFE	UIEBD			Raindrop			LOL-v2		
		PSNR↑	SSIM↑	LPIPS↓	PSNR↑	SSIM↑	LPIPS↓	PSNR↑	SSIM↑	LPIPS↓
Baseline	10	25.08	0.913	0.162	33.32	0.938	0.044	29.54	0.898	0.086
CM [33]	1	25.65	0.904	0.183	33.09	0.933	0.049	29.50	0.882	0.105
CTM [151]	1	25.84	0.919	0.164	33.17	0.936	0.048	29.56	0.884	0.101
Proposed Method	1	26.25	0.938	0.128	33.63	0.946	0.052	29.91	0.904	0.101

image restoration.

Text Conditioning Analysis. Given FLUX’s text-to-image nature, we examined text prompting effects on restoration performance. Table XIV compares three strategies, i.e., no prompt, generic prompt (“a high-quality image” for all tasks), and task-specific prompt (e.g., “high-resolution, ultra-sharp, detailed” for super-resolution). It can be seen that both generic and task-specific prompts demonstrate improvements in perceptual metrics relative to the no-prompt baseline, with task-specific prompts yielding superior performance, indicating that FLUX’s text understanding capabilities can be effectively leveraged for image restoration, with appropriate text guidance helping steer the model toward better perceptual quality. Based on these findings, we adopt task-specific prompts in our unified FLUX-IR framework.

VI. CONCLUSION

We have presented an efficient yet effective trajectory optimization paradigm for image restoration-based diffusion models. Through reinforcement learning-based trajectory augmentation techniques, we boost the effectiveness of the image restoration diffusion network. By employing different reward functions, we can flexibly guide the learning of the diffusion model toward either more objective or perceptual restoration. Moreover, on the basis of distillation cost analysis, we introduced a diffusion acceleration distillation pipeline with several techniques to perverse the original knowledge of diffusion models and achieve single-step distillation. We have carried out extensive experiments on both task-specific image restoration diffusion and unified image restoration diffusion networks over more than 7 different image restoration tasks to validate the effectiveness of the proposed method. Moreover, we have also calibrated a 12B rectified flow-based model for the image restoration task. The experimental results demonstrate the effectiveness of the proposed method, which generates clear and meaningful results compared to the state-of-the-art methods. We believe that our insights and findings would push the frontier of image restoration.

TABLE XIV
RESULTS OF THE ABLATION STUDY ON TEXT PROMPTS OF THE UNIFIED FLUX-IR FRAMEWORK.

Text Prompt	Super-resolution (DIV2K-Val)				Low-light Enhancement (LOL)			
	NIQE↓	MUSIQ↑	CLIPQA↑	PSNR↑	NIQE↓	MUSIQ↑	CLIPQA↑	PSNR↑
No prompt	4.093	67.481	0.602	21.467	4.172	72.939	0.478	24.918
Generic prompt	3.872	68.942	0.640	21.536	4.193	73.605	0.498	24.616
Task-specific prompt	3.491	73.188	0.721	20.248	4.045	73.233	0.484	25.029

Building on the proposed method, promising future work includes developing more advanced reward metrics and integration mechanisms, as well as exploring alternative approaches, such as bridge diffusion, to enhance the model’s controllability and reconstruction fidelity.

REFERENCES

- [1] J. Noh, W. Bae, W. Lee, J. Seo, and G. Kim, “Better to follow, follow to be better: Towards precise supervision of feature super-resolution for small object detection,” in *Proc. IEEE ICCV*, 2019, pp. 9725–9734.
- [2] C. Dong, C. C. Loy, K. He, and X. Tang, “Learning a deep convolutional network for image super-resolution,” in *Proc. ECCV*, 2014, pp. 184–199.
- [3] M. Lu, T. Chen, H. Liu, and Z. Ma, “Learned image restoration for vvc intra coding,” in *Proc. IEEE CVPRW*, vol. 4, 2019.
- [4] M. V. Conde, U.-J. Choi, M. Burchi, and R. Timofte, “Swin2sr: Swinv2 transformer for compressed image super-resolution and restoration,” in *Proc. ECCV*, 2022, pp. 669–687.
- [5] J. Yang, J. Wright, T. S. Huang, and Y. Ma, “Image super-resolution via sparse representation,” *IEEE Transactions on Image Processing*, vol. 19, no. 11, pp. 2861–2873, 2010.
- [6] J. Yang, J. Wright, T. Huang, and Y. Ma, “Image super-resolution as sparse representation of raw image patches,” in *Proc. IEEE CVPR*, 2008, pp. 1–8.
- [7] Y. LeCun, Y. Bengio, and G. Hinton, “Deep learning,” *Nature*, vol. 521, no. 7553, pp. 436–444, 2015.
- [8] C. Dong, C. C. Loy, K. He, and X. Tang, “Image super-resolution using deep convolutional networks,” *IEEE Transactions on Pattern Analysis and Machine Intelligence*, vol. 38, no. 2, pp. 295–307, 2015.
- [9] Y. Zhang, Y. Tian, Y. Kong, B. Zhong, and Y. Fu, “Residual dense network for image super-resolution,” in *Proc. IEEE CVPR*, 2018, pp. 2472–2481.
- [10] S. W. Zamir, A. Arora, S. Khan, M. Hayat, F. S. Khan, and M.-H. Yang, “Restormer: Efficient transformer for high-resolution image restoration,” in *Proc. IEEE CVPR*, 2022, pp. 5728–5739.
- [11] J. Liang, J. Cao, G. Sun, K. Zhang, L. Van Gool, and R. Timofte, “Swinir: Image restoration using swin transformer,” in *Proc. IEEE ICCV*, 2021, pp. 1833–1844.
- [12] C. Ledig, L. Theis, F. Huszár, J. Caballero, A. Cunningham, A. Acosta, A. Aitken, A. Tejani, J. Totz, Z. Wang *et al.*, “Photo-realistic single image super-resolution using a generative adversarial network,” in *Proc. IEEE CVPR*, 2017, pp. 4681–4690.
- [13] X. Wang, K. Yu, S. Wu, J. Gu, Y. Liu, C. Dong, Y. Qiao, and C. Change Loy, “EsrGAN: Enhanced super-resolution generative adversarial networks,” in *Proc. ECCVW*, 2018.
- [14] V. Monga, Y. Li, and Y. C. Eldar, “Algorithm unrolling: Interpretable, efficient deep learning for signal and image processing,” *IEEE Signal Processing Magazine*, vol. 38, no. 2, pp. 18–44, 2021.
- [15] K. Zhang, L. V. Gool, and R. Timofte, “Deep unfolding network for image super-resolution,” in *Proc. IEEE CVPR*, 2020, pp. 3217–3226.
- [16] I. Marivani, E. Tsiliogianni, B. Cornelis, and N. Deligiannis, “Multimodal deep unfolding for guided image super-resolution,” *IEEE Transactions on Image Processing*, vol. 29, pp. 8443–8456, 2020.
- [17] A. Lugmayr, M. Danelljan, L. Van Gool, and R. Timofte, “SrfFlow: Learning the super-resolution space with normalizing flow,” in *Proc. ECCV*, 2020, pp. 715–732.
- [18] Y. Kim and D. Son, “Noise conditional flow model for learning the super-resolution space,” in *Proc. IEEE CVPR*, 2021, pp. 424–432.
- [19] J. Liang, A. Lugmayr, K. Zhang, M. Danelljan, L. Van Gool, and R. Timofte, “Hierarchical conditional flow: A unified framework for image super-resolution and image rescaling,” in *Proc. IEEE ICCV*, 2021, pp. 4076–4085.
- [20] B. Xia, Y. Zhang, S. Wang, Y. Wang, X. Wu, Y. Tian, W. Yang, and L. Van Gool, “Diffir: Efficient diffusion model for image restoration,” in *Proc. IEEE ICCV*, 2023, pp. 13 095–13 105.

- [21] C. Saharia, J. Ho, W. Chan, T. Salimans, D. J. Fleet, and M. Norouzi, “Image super-resolution via iterative refinement,” *IEEE Transactions on Pattern Analysis and Machine Intelligence*, vol. 45, no. 4, pp. 4713–4726, 2022.
- [22] J. Ho, A. Jain, and P. Abbeel, “Denoising diffusion probabilistic models,” in *Proc. NeurIPS*, 2020, pp. 6840–6851.
- [23] B. D. Anderson, “Reverse-time diffusion equation models,” *Stochastic Processes and their Applications*, vol. 12, no. 3, pp. 313–326, 1982.
- [24] Y. Song, J. Sohl-Dickstein, D. P. Kingma, A. Kumar, S. Ermon, and B. Poole, “Score-based generative modeling through stochastic differential equations,” in *Proc. ICLR*, 2021, pp. 1–12.
- [25] B. Kawar, M. Elad, S. Ermon, and J. Song, “Denoising diffusion restoration models,” in *Proc. NeurIPS*, vol. 35, 2022, pp. 23 593–23 606.
- [26] H. Chung, J. Kim, M. T. Mccann, M. L. Klasky, and J. C. Ye, “Diffusion posterior sampling for general noisy inverse problems,” in *Proc. ICLR*, 2023, pp. 1–12.
- [27] Y. Wang, J. Yu, and J. Zhang, “Zero-shot image restoration using denoising diffusion null-space model,” in *Proc. ICLR*, 2023.
- [28] B. Fei, Z. Lyu, L. Pan, J. Zhang, W. Yang, T. Luo, B. Zhang, and B. Dai, “Generative diffusion prior for unified image restoration and enhancement,” in *Proc. IEEE CVPR*, 2023, pp. 9935–9946.
- [29] Z. Luo, F. K. Gustafsson, Z. Zhao, J. Sjölund, and T. B. Schön, “Image restoration with mean-reverting stochastic differential equations,” in *Proc. ICML*, vol. 202, 2023, pp. 23 045–23 066.
- [30] J. Wang, Z. Yue, S. Zhou, K. C. Chan, and C. C. Loy, “Exploiting diffusion prior for real-world image super-resolution,” *International Journal of Computer Vision*, vol. 132, no. 12, pp. 5929–5949, 2024.
- [31] H. Chung, J. Kim, and J. C. Ye, “Direct diffusion bridge using data consistency for inverse problems,” in *Proc. NeurIPS*, vol. 36, 2024.
- [32] X. Liu, C. Gong, and qiang liu, “Flow straight and fast: Learning to generate and transfer data with rectified flow,” in *Proc. ICLR*, 2023.
- [33] Y. Song, P. Dhariwal, M. Chen, and I. Sutskever, “Consistency models,” in *Proc. ICML*, vol. 202, 2023, pp. 32 211–32 252.
- [34] J. Sohl-Dickstein, E. Weiss, N. Maheswaranathan, and S. Ganguli, “Deep unsupervised learning using nonequilibrium thermodynamics,” in *Proc. ICML*, 2015, pp. 2256–2265.
- [35] Y. Song and S. Ermon, “Generative modeling by estimating gradients of the data distribution,” in *Proc. NeurIPS*, vol. 32, 2019.
- [36] Y. Song and S. . Ermon, “Improved techniques for training score-based generative models,” in *Proc. NeurIPS*, vol. 33, 2020, pp. 12 438–12 448.
- [37] Y. Song, C. Durkan, I. Murray, and S. Ermon, “Maximum likelihood training of score-based diffusion models,” in *Proc. NeurIPS*, vol. 34, 2021, pp. 1415–1428.
- [38] C. Lu, Y. Zhou, F. Bao, J. Chen, C. Li, and J. Zhu, “Dpm-solver: A fast ode solver for diffusion probabilistic model sampling in around 10 steps,” in *Proc. NeurIPS*, vol. 35, 2022, pp. 5775–5787.
- [39] C. Lu, Y. Zhou, F. Bao, J. Chen, C. Li, and J. . Zhu, “Dpm-solver++: Fast solver for guided sampling of diffusion probabilistic models,” *arXiv preprint arXiv:2211.01095*, 2022.
- [40] K. Zheng, C. Lu, J. Chen, and J. Zhu, “Dpm-solver-v3: Improved diffusion ode solver with empirical model statistics,” in *Proc. NeurIPS*, vol. 36, 2024, pp. 55 502–55 542.
- [41] Y. Xu, Z. Liu, M. Tegmark, and T. Jaakkola, “Poisson flow generative models,” in *Proc. NeurIPS*, vol. 35, 2022, pp. 16 782–16 795.
- [42] R. Rombach, A. Blattmann, D. Lorenz, P. Esser, and B. Ommer, “High-resolution image synthesis with latent diffusion models,” in *Proc. IEEE CVPR*, 2022, pp. 10 684–10 695.
- [43] A. Blattmann, T. Dockhorn, S. Kulal, D. Mendelevitch, M. Kilian, D. Lorenz, Y. Levi, Z. English, V. Voleti, A. Letts *et al.*, “Stable video diffusion: Scaling latent video diffusion models to large datasets,” *arXiv preprint arXiv:2311.15127*, 2023.
- [44] A. Blattmann, R. Rombach, H. Ling, T. Dockhorn, S. W. Kim, S. Fidler, and K. Kreis, “Align your latents: High-resolution video synthesis with latent diffusion models,” in *Proc. IEEE CVPR*, 2023, pp. 22 563–22 575.
- [45] T. Karras, M. Aittala, T. Aila, and S. Laine, “Elucidating the design space of diffusion-based generative models,” in *Proc. NeurIPS*, vol. 35, 2022, pp. 26 565–26 577.
- [46] T. Dockhorn, A. Vahdat, and K. Kreis, “Score-based generative modeling with critically-damped langevin diffusion,” in *Proc. ICLR*, 2022.
- [47] S. Chen, S. Chewi, J. Li, Y. Li, A. Salim, and A. Zhang, “Sampling is as easy as learning the score: theory for diffusion models with minimal data assumptions,” in *Proc. ICLR*, 2023.
- [48] X. Liu, L. Wu, M. Ye, and Q. Liu, “Let us build bridges: Understanding and extending diffusion generative models,” *arXiv preprint arXiv:2208.14699*, 2022.
- [49] B. Li, K. Xue, B. Liu, and Y.-K. Lai, “Bbdm: Image-to-image translation with brownian bridge diffusion models,” in *Proc. IEEE CVPR*, 2023, pp. 1952–1961.
- [50] L. Zhou, A. Lou, S. Khanna, and S. Ermon, “Denoising diffusion bridge models,” in *Proc. ICLR*.
- [51] J. Song, C. Meng, and S. Ermon, “Denoising diffusion implicit models,” in *Proc. ICLR*, 2021, pp. 1–12.
- [52] Q. Zhang and Y. Chen, “Fast sampling of diffusion models with exponential integrator,” *arXiv preprint arXiv:2204.13902*, 2022.
- [53] Z. Zhou, D. Chen, C. Wang, and C. Chen, “Fast ode-based sampling for diffusion models in around 5 steps,” in *Proc. IEEE CVPR*, 2024, pp. 7777–7786.
- [54] S. Xue, M. Yi, W. Luo, S. Zhang, J. Sun, Z. Li, and Z.-M. Ma, “Sasolver: Stochastic adams solver for fast sampling of diffusion models,” in *Proc. NeurIPS*, vol. 36, 2023, pp. 77 632–77 674.
- [55] S. Xue, Z. Liu, F. Chen, S. Zhang, T. Hu, E. Xie, and Z. Li, “Accelerating diffusion sampling with optimized time steps,” in *Proc. IEEE CVPR*, 2024, pp. 8292–8301.
- [56] T. Dockhorn, A. Vahdat, and K. Kreis, “Genie: Higher-order denoising diffusion solvers,” in *Proc. NeurIPS*, vol. 35, 2022, pp. 30 150–30 166.
- [57] Y. Song and P. Dhariwal, “Improved techniques for training consistency models,” in *Proc. ICLR*, 2023.
- [58] D. Kim, C.-H. Lai, W.-H. Liao, N. Murata, Y. Takida, T. Uesaka, Y. He, Y. Mitsuishi, and S. Ermon, “Consistency trajectory models: Learning probability flow ode trajectory of diffusion,” in *Proc. ICLR*, 2024.
- [59] M. Zhou, H. Zheng, Z. Wang, M. Yin, and H. Huang, “Score identity distillation: Exponentially fast distillation of pretrained diffusion models for one-step generation,” in *Proc. ICML*, 2024, pp. 62 307–62 331.
- [60] M. Zhou, Z. Wang, H. Zheng, and H. Huang, “Long and short guidance in score identity distillation for one-step text-to-image generation,” *arXiv 2406.01561*, 2024.
- [61] Y. Ren, X. Xia, Y. Lu, J. Zhang, J. Wu, P. Xie, X. Wang, and X. Xiao, “Hyper-sd: Trajectory segmented consistency model for efficient image synthesis,” *arXiv preprint arXiv:2404.13686*, 2024.
- [62] F.-Y. Wang, Z. Huang, A. W. Bergman, D. Shen, P. Gao, M. Lingelbach, K. Sun, W. Bian, G. Song, Y. Liu *et al.*, “Phased consistency model,” *arXiv preprint arXiv:2405.18407*, 2024.
- [63] Q. Xie, Z. Liao, Z. Deng, S. Tang, H. Lu *et al.*, “Mlcml: Multi-step consistency distillation of latent diffusion model,” *arXiv preprint arXiv:2406.05768*, 2024.
- [64] Y. Zhu, K. Zhang, J. Liang, J. Cao, B. Wen, R. Timofte, and L. Van Gool, “Denoising diffusion models for plug-and-play image restoration,” in *Proc. IEEE CVPR*, 2023, pp. 1219–1229.
- [65] O. Özdenizci and R. Legenstein, “Restoring vision in adverse weather conditions with patch-based denoising diffusion models,” *IEEE Transactions on Pattern Analysis and Machine Intelligence*, vol. 45, no. 8, pp. 10 346–10 357, 2023.
- [66] Y. Zhang, X. Shi, D. Li, X. Wang, J. Wang, and H. Li, “A unified conditional framework for diffusion-based image restoration,” in *Proc. NeurIPS*, vol. 36, 2024, pp. 49 703–49 714.
- [67] Z. Luo, F. K. Gustafsson, Z. Zhao, J. Sjölund, and T. B. Schön, “Refusion: Enabling large-size realistic image restoration with latent-space diffusion models,” in *Proc. IEEE CVPR*, 2023, pp. 1680–1691.
- [68] Z. Luo, F. K. Gustafsson, Z. Zhao, and et al., “Controlling vision-language models for multi-task image restoration,” in *Proc. ICLR*, 2024, pp. 1–13.
- [69] H. Jiang, A. Luo, H. Fan, S. Han, and S. Liu, “Low-light image enhancement with wavelet-based diffusion models,” *ACM Transactions on Graphics*, vol. 42, no. 6, pp. 1–14, 2023.
- [70] X. Yi, H. Xu, H. Zhang, L. Tang, and J. Ma, “Diff-retinex: Rethinking low-light image enhancement with a generative diffusion model,” in *Proc. IEEE ICCV*, 2023, pp. 12 302–12 311.
- [71] Y. Wang, W. Yang, X. Chen, Y. Wang, L. Guo, L.-P. Chau, Z. Liu, Y. Qiao, A. C. Kot, and B. Wen, “Sinsr: diffusion-based image super-resolution in a single step,” in *Proc. IEEE CVPR*, 2024, pp. 25 796–25 805.
- [72] Y. Tang, H. Kawasaki, and T. Iwaguchi, “Underwater image enhancement by transformer-based diffusion model with non-uniform sampling for skip strategy,” in *Proc. ACM MM*, 2023, pp. 5419–5427.
- [73] V. Potlapalli, S. W. Zamir, S. Khan, and F. Khan, “Promptir: Prompting for all-in-one image restoration,” in *Proc. NeurIPS*, 2023, pp. 71 275–71 293.
- [74] X. Lin, J. He, Z. Chen, Z. Lyu, B. Dai, F. Yu, Y. Qiao, W. Ouyang, and C. Dong, “Diffbir: Toward blind image restoration with generative diffusion prior,” in *Proc. ECCV*, 2024, pp. 430–448.

- [75] Y. Jiang, Z. Zhang, T. Xue, and J. Gu, “Autodir: Automatic all-in-one image restoration with latent diffusion,” in *Proc. ECCV*, 2024, pp. 340–359.
- [76] Y. Cui, S. W. Zamir, S. Khan, A. Knoll, M. Shah, and F. S. Khan, “AdaIR: Adaptive all-in-one image restoration via frequency mining and modulation,” in *Proc. ICLR*, 2025.
- [77] Q. Yan, A. Jiang, K. Chen, L. Peng, Q. Yi, and C. Zhang, “Textual prompt guided image restoration,” *arXiv preprint arXiv:2312.06162*, 2024.
- [78] D. Zheng, X.-M. Wu, S. Yang, J. Zhang, J.-F. Hu, and W.-S. Zheng, “Selective hourglass mapping for universal image restoration based on diffusion model,” in *Proc. IEEE CVPR*, 2024, pp. 25 445–25 455.
- [79] Y. Ai, H. Huang, X. Zhou, J. Wang, and R. He, “Multimodal prompt perceiver: Empower adaptiveness generalizability and fidelity for all-in-one image restoration,” in *Proc. IEEE CVPR*, 2024, pp. 25 432–25 444.
- [80] M. V. Conde, G. Geigle, and R. Timofte, “Instructir: High-quality image restoration following human instructions,” in *Proc. ECCV*, 2024, pp. 1–21.
- [81] X. Yu, S. Zhou, H. Li, and L. Zhu, “Multi-expert adaptive selection: Task-balancing for all-in-one image restoration,” *arXiv preprint arXiv:2407.19139*, 2024.
- [82] Y. Zhang, H. Zhang, X. Chai, Z. Cheng, R. Xie, L. Song, and W. Zhang, “Diff-restorer: Unleashing visual prompts for diffusion-based universal image restoration,” *arXiv preprint arXiv:2407.03636*, 2024.
- [83] Y. Luo, R. Zhao, X. Wei, J. Chen, Y. Lu, S. Xie, T. Wang, R. Xiong, M. Lu, and S. Zhang, “Wm-moe: Weather-aware multi-scale mixture-of-experts for blind adverse weather removal,” *arXiv preprint arXiv:2303.13739*, 2024.
- [84] J. Jiang, Z. Zuo, G. Wu, K. Jiang, and X. Liu, “A survey on all-in-one image restoration: Taxonomy, evaluation and future trends,” *arXiv preprint arXiv:2410.15067*, 2024.
- [85] C. Meng, R. Rombach, R. Gao, D. Kingma, S. Ermon, J. Ho, and T. Salimans, “On distillation of guided diffusion models,” in *Proc. IEEE CVPR*, 2023, pp. 14 297–14 306.
- [86] R. Zhang, P. Isola, A. A. Efros, E. Shechtman, and O. Wang, “The unreasonable effectiveness of deep features as a perceptual metric,” in *Proc. IEEE CVPR*, 2018, pp. 586–595.
- [87] Y. Fan, O. Watkins, Y. Du, H. Liu, M. Ryu, C. Boutilier, P. Abbeel, M. Ghavamzadeh, K. Lee, and K. Lee, “Dpk: Reinforcement learning for fine-tuning text-to-image diffusion models,” in *Proc. NeurIPS*, vol. 36, 2023, pp. 79 858–79 885.
- [88] B. Wallace, M. Dang, R. Rafailov, L. Zhou, A. Lou, S. Purushwalkam, S. Ermon, C. Xiong, S. Joty, and N. Naik, “Diffusion model alignment using direct preference optimization,” in *Proc. IEEE CVPR*, 2024, pp. 8228–8238.
- [89] L. P. Kaelbling, M. L. Littman, and A. W. Moore, “Reinforcement learning: A survey,” *Journal of Artificial Intelligence Research*, vol. 4, pp. 237–285, 1996.
- [90] M. A. Wiering and M. Van Otterlo, “Reinforcement learning.” *Adaptation, Learning, and Optimization*, vol. 12, no. 3, p. 729, 2012.
- [91] Q. Zhang and Y. Chen, “Diffusion normalizing flow,” in *Proc. NeurIPS*, vol. 34, 2021, pp. 16 280–16 291.
- [92] X. Liu, X. Zhang, J. Ma, J. Peng *et al.*, “Instaflow: One step is enough for high-quality diffusion-based text-to-image generation,” in *Proc. ICLR*, 2024, pp. 1–16.
- [93] A. Sauer, D. Lorenz, A. Blattmann, and R. Rombach, “Adversarial diffusion distillation,” *arXiv preprint arXiv:2311.17042*, 2023.
- [94] C. Ancuti, C. O. Ancuti, T. Haber, and P. Bekaert, “Enhancing underwater images and videos by fusion,” in *Proc. IEEE CVPR*, 2012, pp. 81–88.
- [95] C. Li, C. Guo, W. Ren, R. Cong, J. Hou, S. Kwong, and D. Tao, “An underwater image enhancement benchmark dataset and beyond,” *IEEE Transactions on Image Processing*, vol. 29, pp. 4376–4389, 2019.
- [96] J.-Y. Zhu, T. Park, P. Isola, and A. A. Efros, “Unpaired image-to-image translation using cycle-consistent adversarial networks,” in *Proc. IEEE ICCV*, 2017, pp. 2223–2232.
- [97] W. Zhang, P. Zhuang, H.-H. Sun, G. Li, S. Kwong, and C. Li, “Underwater image enhancement via minimal color loss and locally adaptive contrast enhancement,” *IEEE Transactions on Image Processing*, vol. 31, pp. 3997–4010, 2022.
- [98] J. Zhou, J. Sun, C. Li, Q. Jiang, M. Zhou, K.-M. Lam, W. Zhang, and X. Fu, “Hclr-net: Hybrid contrastive learning regularization with locally randomized perturbation for underwater image enhancement,” *International Journal of Computer Vision*, vol. 132, no. 10, pp. 4132–4156, 2024.
- [99] S. Huang, K. Wang, H. Liu, J. Chen, and Y. Li, “Contrastive semi-supervised learning for underwater image restoration via reliable bank,” in *Proc. IEEE CVPR*, 2023, pp. 18 145–18 155.
- [100] C. Li, S. Anwar, J. Hou, R. Cong, C. Guo, and W. Ren, “Underwater image enhancement via medium transmission-guided multi-color space embedding,” *IEEE Transactions on Image Processing*, vol. 30, pp. 4985–5000, 2021.
- [101] L. Chen, X. Chu, X. Zhang, and J. Sun, “Simple baselines for image restoration,” in *Proc. ECCV*, 2022, pp. 17–33.
- [102] Y. Feng, C. Zhang, P. Wang, P. Wu, Q. Yan, and Y. Zhang, “You only need one color space: An efficient network for low-light image enhancement,” *arXiv preprint arXiv:2402.05809*, 2024.
- [103] Y. Wang, R. Wan, W. Yang, H. Li, L.-P. Chau, and A. Kot, “Low-light image enhancement with normalizing flow,” in *Proc. AAAI*, vol. 36, no. 3, 2022, pp. 2604–2612.
- [104] Y. Cai, H. Bian, J. Lin, H. Wang, R. Timofte, and Y. Zhang, “Retinex-former: One-stage retinex-based transformer for low-light image enhancement,” in *Proc. IEEE ICCV*, 2023, pp. 12 504–12 513.
- [105] T. Wang, K. Zhang, T. Shen, W. Luo, B. Stenger, and T. Lu, “Ultra-high-definition low-light image enhancement: A benchmark and transformer-based method,” in *Proc. AAAI*, vol. 37, no. 3, 2023, pp. 2654–2662.
- [106] X. Xu, R. Wang, C.-W. Fu, and J. Jia, “Snr-aware low-light image enhancement,” in *Proc. IEEE CVPR*, 2022, pp. 17 714–17 724.
- [107] C. Guo, C. Li, J. Guo, C. C. Loy, J. Hou, S. Kwong, and R. Cong, “Zero-reference deep curve estimation for low-light image enhancement,” in *Proc. IEEE CVPR*, 2020, pp. 1780–1789.
- [108] Y. Jiang, X. Gong, D. Liu, Y. Cheng, C. Fang, X. Shen, J. Yang, P. Zhou, and Z. Wang, “Enlightengan: Deep light enhancement without paired supervision,” *IEEE Transactions on Image Processing*, vol. 30, pp. 2340–2349, 2021.
- [109] C. Wei, W. Wang, W. Yang, and J. Liu, “Deep retinex decomposition for low-light enhancement,” in *Proc. BMVC*, 2018.
- [110] W. Yang, S. Wang, Y. Fang, Y. Wang, and J. Liu, “From fidelity to perceptual quality: A semi-supervised approach for low-light image enhancement,” in *Proc. IEEE CVPR*, 2020, pp. 3063–3072.
- [111] Y. Zhang, J. Zhang, and X. Guo, “Kindling the darkness: A practical low-light image enhancer,” in *Proc. ACM MM*, 2019, pp. 1632–1640.
- [112] Y. Zhang, X. Guo, J. Ma, W. Liu, and J. Zhang, “Beyond brightening low-light images,” *International Journal of Computer Vision*, vol. 129, pp. 1013–1037, 2021.
- [113] S. W. Zamir, A. Arora, S. Khan, M. Hayat, F. S. Khan, M.-H. Yang, and L. Shao, “Learning enriched features for fast image restoration and enhancement,” *IEEE Transactions on Pattern Analysis and Machine Intelligence*, vol. 45, no. 2, pp. 1934–1948, 2022.
- [114] D. Zhou, Z. Yang, and Y. Yang, “Pyramid diffusion models for low-light image enhancement,” in *Proc. IJCAI*, 2023, pp. 1795–1803.
- [115] Y. Wu, G. Wang, S. Liu, Y. Yang, W. Li, X. Tang, S. Gu, C. Li, and H. T. Shen, “Towards a flexible semantic guided model for single image enhancement and restoration,” *IEEE Transactions on Pattern Analysis and Machine Intelligence*, vol. 46, no. 12, pp. 9921–9939, 2024.
- [116] J. Hou, Z. Zhu, J. Hou, H. Liu, H. Zeng, and H. Yuan, “Global structure-aware diffusion process for low-light image enhancement,” in *Proc. NeurIPS*, vol. 36, 2023, pp. 79 734–79 747.
- [117] B. Andreas, S. Axel, L. Dominik, P. Dustin, B. Frederic, S. Harry, M. Jonas, L. Kyle, E. Patrick, R. Robin, K. Sumith, D. Tim, L. Yam, and E. Zion, “Flux,” 2024. [Online]. Available: <https://blackforestlabs.ai/>
- [118] H. Li, J. Li, and W. Wang, “A fusion adversarial underwater image enhancement network with a public test dataset,” *arXiv preprint arXiv:1906.06819*, 2019.
- [119] W. Yang, W. Wang, H. Huang, S. Wang, and J. Liu, “Sparse gradient regularized deep retinex network for robust low-light image enhancement,” *IEEE Transactions on Image Processing*, vol. 30, pp. 2072–2086, 2021.
- [120] R. Qian, R. T. Tan, W. Yang, J. Su, and J. Liu, “Attentive generative adversarial network for raindrop removal from a single image,” in *Proc. IEEE CVPR*, 2018, pp. 2482–2491.
- [121] K. Jiang, Z. Wang, P. Yi, C. Chen, B. Huang, Y. Luo, J. Ma, and J. Jiang, “Multi-scale progressive fusion network for single image deraining,” in *Proc. IEEE CVPR*, 2020, pp. 8346–8355.
- [122] W. Yang, R. T. Tan, J. Feng, J. Liu, Z. Guo, and S. Yan, “Deep joint rain detection and removal from a single image,” in *Proc. IEEE CVPR*, 2017, pp. 1357–1366.
- [123] H. Zhang and V. M. Patel, “Density-aware single image de-raining using a multi-stream dense network,” in *Proc. IEEE CVPR*, 2018, pp. 695–704.

- [124] X. Fu, J. Huang, D. Zeng, Y. Huang, X. Ding, and J. Paisley, “Removing rain from single images via a deep detail network,” in *Proc. IEEE CVPR*, 2017, pp. 3855–3863.
- [125] E. Agustsson and R. Timofte, “Ntire 2017 challenge on single image super-resolution: Dataset and study,” in *Proc. IEEE CVPRW*, 2017.
- [126] B. Lim, S. Son, H. Kim, S. Nah, and K. Mu Lee, “Enhanced deep residual networks for single image super-resolution,” in *Proc. IEEE CVPRW*, 2017, pp. 136–144.
- [127] X. Wang, L. Xie, C. Dong, and Y. Shan, “Real-esrgan: Training real-world blind super-resolution with pure synthetic data,” in *Proc. IEEE ICCV*, 2021, pp. 1905–1914.
- [128] Y.-F. Liu, D.-W. Jaw, S.-C. Huang, and J.-N. Hwang, “Desnownet: Context-aware deep network for snow removal,” *IEEE Transactions on Image Processing*, vol. 27, no. 6, pp. 3064–3073, 2018.
- [129] S. Nah, T. Hyun Kim, and K. Mu Lee, “Deep multi-scale convolutional neural network for dynamic scene deblurring,” in *Proc. IEEE CVPR*, 2017, pp. 3883–3891.
- [130] P. Arbelaez, M. Maire, C. Fowlkes, and J. Malik, “Contour detection and hierarchical image segmentation,” *IEEE Transactions on Pattern Analysis and Machine Intelligence*, vol. 33, no. 5, pp. 898–916, 2010.
- [131] A. Abdelhamed, S. Lin, and M. S. Brown, “A high-quality denoising dataset for smartphone cameras,” in *Proc. IEEE CVPR*, 2018, pp. 1692–1700.
- [132] A. Mittal, R. Soundararajan, and A. C. Bovik, “Making a “completely blind” image quality analyzer,” *IEEE Signal Processing Letters*, vol. 20, no. 3, pp. 209–212, 2012.
- [133] J. Ke, Q. Wang, Y. Wang, P. Milanfar, and F. Yang, “Musiq: Multi-scale image quality transformer,” in *Proc. IEEE ICCV*, 2021, pp. 5148–5157.
- [134] J. Wang, K. C. Chan, and C. C. Loy, “Exploring clip for assessing the look and feel of images,” in *Proc. AAAI*, vol. 37, no. 2, 2023, pp. 2555–2563.
- [135] J. Xiao, X. Fu, A. Liu, F. Wu, and Z.-J. Zha, “Image de-raining transformer,” *IEEE Transactions on Pattern Analysis and Machine Intelligence*, vol. 45, no. 11, pp. 12978–12995, 2022.
- [136] T. Wang, K. Zhang, Z. Shao, W. Luo, B. Stenger, T. Lu, T.-K. Kim, W. Liu, and H. Li, “Gridformer: Residual dense transformer with grid structure for image restoration in adverse weather conditions,” *International Journal of Computer Vision*, pp. 1–23, 2024.
- [137] P. Isola, J.-Y. Zhu, T. Zhou, and A. A. Efros, “Image-to-image translation with conditional adversarial networks,” in *Proc. IEEE CVPR*, 2017, pp. 1125–1134.
- [138] R. Li, L.-F. Cheong, and R. T. Tan, “Heavy rain image restoration: Integrating physics model and conditional adversarial learning,” in *Proc. IEEE CVPR*, 2019, pp. 1633–1642.
- [139] K. Jiang, Z. Wang, P. Yi, C. Chen, Z. Wang, X. Wang, J. Jiang, and C.-W. Lin, “Rain-free and residue hand-in-hand: A progressive coupled network for real-time image deraining,” *IEEE Transactions on Image Processing*, vol. 30, pp. 7404–7418, 2021.
- [140] S. W. Zamir, A. Arora, S. Khan, M. Hayat, F. S. Khan, M.-H. Yang, and L. Shao, “Multi-stage progressive image restoration,” in *Proc. IEEE CVPR*, 2021, pp. 14821–14831.
- [141] T. Ye, S. Chen, W. Chai, Z. Xing, J. Qin, G. Lin, and L. Zhu, “Learning diffusion texture priors for image restoration,” in *Proc. IEEE CVPR*, 2024, pp. 2524–2534.
- [142] X. Liu, M. Suganuma, Z. Sun, and T. Okatani, “Dual residual networks leveraging the potential of paired operations for image restoration,” in *Proc. IEEE CVPR*, 2019, pp. 7007–7016.
- [143] Y. Quan, S. Deng, Y. Chen, and H. Ji, “Deep learning for seeing through window with raindrops,” in *Proc. IEEE ICCV*, 2019, pp. 2463–2471.
- [144] S. Zhou, D. Chen, J. Pan, J. Shi, and J. Yang, “Adapt or perish: Adaptive sparse transformer with attentive feature refinement for image restoration,” in *Proc. IEEE CVPR*, 2024, pp. 2952–2963.
- [145] T. Yang, R. Wu, P. Ren, X. Xie, and L. Zhang, “Pixel-aware stable diffusion for realistic image super-resolution and personalized stylization,” in *Proc. ECCV*, 2024, pp. 74–91.
- [146] R. Wu, T. Yang, L. Sun, Z. Zhang, S. Li, and L. Zhang, “Seesr: Towards semantics-aware real-world image super-resolution,” in *Proc. IEEE CVPR*, 2024, pp. 25456–25467.
- [147] Y. Zhu, T. Wang, X. Fu, X. Yang, X. Guo, J. Dai, Y. Qiao, and X. Hu, “Learning weather-general and weather-specific features for image restoration under multiple adverse weather conditions,” in *Proc. IEEE CVPR*, 2023, pp. 21747–21758.
- [148] X. Chen, H. Li, M. Li, and J. Pan, “Learning a sparse transformer network for effective image deraining,” in *Proc. IEEE CVPR*, 2023, pp. 5896–5905.
- [149] N. Gao, X. Jiang, X. Zhang, and Y. Deng, “Efficient frequency-domain image deraining with contrastive regularization,” in *Proc. ECCV*, 2024, pp. 240–257.
- [150] C. Guo, R. Wu, X. Jin, L. Han, W. Zhang, Z. Chai, and C. Li, “Underwater ranker: Learn which is better and how to be better,” in *Proc. AAAI*, vol. 37, no. 1, 2023, pp. 702–709.
- [151] D. Kim, C.-H. Lai, W.-H. Liao, N. Murata, Y. Takida, T. Uesaka, Y. He, Y. Mitsufuji, and S. Ermon, “Consistency trajectory models: Learning probability flow ode trajectory of diffusion,” in *Proc. ICLR*, 2024.
- [152] “Xflux,” 2024. [Online]. Available: <https://github.com/XLabs-AI/x-flux>



Zhiyu Zhu received the B.E. and M.E. degrees in Mechatronic Engineering, both from Harbin Institute of Technology, in 2017 and 2019, respectively. He has also received a Ph.D. degree in Computer Science from the City University of Hong Kong in 2023, where he currently holds a postdoctoral position. His research interests include generative models and computer vision.



Jinhui Hou received the B.E. and M.E. degrees in Communication Engineering from Huaqiao University, Xiamen, China, in 2017 and 2020, respectively. He is pursuing a Ph.D. in Computer Science at the City University of Hong Kong. His research interests include image processing and computer vision.



Hui Liu is currently an Assistant Professor in the School of Computing and Information Sciences at Saint Francis University, Hong Kong. She received the B.Sc. degree in Communication Engineering from Central South University, Changsha, China, the M.Eng. degree in Computer Science from Nanyang Technological University, Singapore, and the Ph.D. degree from the Department of Computer Science, City University of Hong Kong, Hong Kong. Her research interests include image processing and machine learning.



Huaiqiang Zeng received the B.S. and M.S. degrees in electrical engineering from Huaqiao University, China, and the Ph.D. degree in electrical engineering from Nanyang Technological University, Singapore.

He is currently a Full Professor at the School of Engineering and the School of Information Science and Engineering, Huaqiao University. He has been actively serving as an Associate Editor for *IEEE Transactions on Image Processing*, *IEEE Transactions on Circuits and Systems for Video Technology*, and *Electronics Letters (IET)*. He has been actively serving as a Guest Editor for *Journal of Visual Communication and Image Representation*, *Multimedia Tools and Applications*, and *Journal of Ambient Intelligence and Humanized Computing*.



Junhui Hou (Senior Member, IEEE) is an Associate Professor with the Department of Computer Science, City University of Hong Kong. He holds a B.Eng. degree in information engineering (Talented Students Program) from the South China University of Technology, Guangzhou, China (2009), an M.Eng. degree in signal and information processing from Northwestern Polytechnical University, Xi'an, China (2012), and a Ph.D. degree from the School of Electrical and Electronic Engineering, Nanyang Technological University, Singapore (2016). His research interests are multi-dimensional visual computing.

Dr. Hou received the Early Career Award (3/381) from the Hong Kong Research Grants Council in 2018 and the NSFC Excellent Young Scientists Fund in 2024. He has served or is serving as an Associate Editor for *IEEE Transactions on Visualization and Computer Graphics*, *IEEE Transactions on Image Processing*, *IEEE Transactions on Multimedia*, and *IEEE Transactions on Circuits and Systems for Video Technology*.

Learning Efficient and Effective Trajectories for Differential Equation-based Image Restoration

(Supplementary Material)

Zhiyu Zhu, Jinhui Hou, Hui Liu, Huanqiang Zeng, and Junhui Hou, *Senior Member, IEEE*

I. ADAPTIVELY ADJUSTING NOISE INTENSITY IS NECESSARY FOR ALIGNMENT OF DIFFUSION TRAJECTORIES

In this section, we analyze that, for a reinforcement alignment process in diffusion models, it is necessary to adaptively adjust the intensity to compensate for the score estimation error. Considering the time-stamp of the to-be-aligned feature map as t , according to the DPM-Solver, we can calculate \mathbf{X}_0 by \mathbf{X}_t as

$$\mathbf{X}_0 = \frac{\alpha_0}{\alpha_t} \mathbf{X}_t + \left(\frac{\sigma_\tau}{\alpha_\tau} \Big|_{\tau=t}^{\tau=0} \right) \alpha_0 \epsilon_\theta(\mathbf{X}_t, t).$$

Then, for the ground-truth \mathbf{X}_0^* , we have

$$\mathbf{X}_0^* = \frac{\alpha_0}{\alpha_t} \mathbf{X}_t^* + \left(\frac{\sigma_\tau}{\alpha_\tau} \Big|_{\tau=t}^{\tau=0} \right) \alpha_0 \epsilon_\theta(\mathbf{X}_t^*, t),$$

where \mathbf{X}_t^* is obtained via adding random perturbation to \mathbf{X}_t , i.e., $\mathbf{X}_t^* = \mathbf{X}_t + \gamma \epsilon$, ($\epsilon \sim \mathcal{N}(\mathbf{0}, \mathbf{I})$). Thus, we have

$$\begin{aligned} & \|\mathbf{X}_0 - \mathbf{X}_0^*\|_2 \\ &= \left\| \frac{\alpha_0}{\alpha_t} (\mathbf{X}_t - \mathbf{X}_t^*) + \left(\frac{\sigma_\tau}{\alpha_\tau} \Big|_{\tau=t}^{\tau=0} \right) \alpha_0 (\epsilon_\theta(\mathbf{X}_t, t) - \epsilon_\theta(\mathbf{X}_t^*, t)) \right\|_2 \\ &\stackrel{\textcircled{1}}{=} \left\| \frac{\alpha_0}{\alpha_t} (\mathbf{X}_t - \mathbf{X}_t^*) + \left(\frac{\sigma_\tau}{\alpha_\tau} \Big|_{\tau=t}^{\tau=0} \right) \alpha_0 k (\mathbf{X}_t - \mathbf{X}_t^*) \right\|_2 \\ &= \left| \frac{\alpha_0}{\alpha_t} + \alpha_0 k \left(\frac{\sigma_\tau}{\alpha_\tau} \Big|_{\tau=t}^{\tau=0} \right) \right| \|\mathbf{X}_t - \mathbf{X}_t^*\|_2, \end{aligned}$$

where $\textcircled{1}$ holds under the assumption that the noise prediction network $\epsilon_\theta(\cdot)$ can accurately predict all the noise. Thus, we have $\epsilon_\theta(\mathbf{X}_t, t) - \epsilon_\theta(\mathbf{X}_t^*, t) \approx k(\mathbf{X}_t - \mathbf{X}_t^*)$ and

$$\|\mathbf{X}_t - \mathbf{X}_t^*\|_2 \approx \frac{\|\mathbf{X}_0 - \mathbf{X}_0^*\|_2}{\left| \frac{\alpha_0}{\alpha_t} - k \alpha_0 \left(\frac{\sigma_\tau}{\alpha_\tau} \Big|_{\tau=0}^{\tau=t} \right) \right|}.$$

Considering the parameterization $\mathbf{X}_t^* = \mathbf{X}_t + \gamma \epsilon$, ($\epsilon \sim \mathcal{N}(\mathbf{0}, \mathbf{I})$), we have $\|\mathbf{X}_t - \mathbf{X}_t^*\|_2 = \gamma$.

Zhiyu Zhu, Jinhui Hou, and Junhui Hou are with the Department of Computer Science, City University of Hong Kong, Hong Kong SAR (e-mail: zhiyuzhu2@my.cityu.edu.hk; jhhou3-c@my.cityu.edu.hk; jh.hou@cityu.edu.hk). Zhiyu Zhu and Jinhui Hou contributed equally to this paper. *Corresponding author: Junhui Hou.*

Hui Liu is with the School of Computing and Information Sciences, Saint Francis University, Hong Kong SAR (e-mail: h2liu@sfsu.edu.hk).

Huanqiang Zeng is with the School of Engineering, Huaqiao University, Quanzhou 362021, China, and also with the School of Information Science and Engineering, Huaqiao University, Xiamen 361021, China (e-mail: zeng0043@hqu.edu.cn).

Based on the above analyses, it can be concluded that γ is correlated with the reconstruction error $\|\mathbf{X}_0 - \mathbf{X}_0^*\|_2$ and the timestamp t to be adjusted. Thus, we parameterize a learnable function $\gamma_\phi(\|\mathbf{X}_0 - \mathbf{X}_0^*\|_2, t)$.

II. MODULATED-SDE AND ITS INTEGRAL SOLVER

A. Modulated-SDE as a General Expression of Reverse Diffusion Derivative Equation

The proof generally follows the diffusion ODE from [1]. Considering a general formulation of forward diffusion SDE as

$$d\mathbf{X} = f(\mathbf{X}, t)dt + g(t)d\omega,$$

the marginal probability $\mathbf{P}(\mathbf{X}_t)$ evolves with the following Kolmogorov's forward equation [2]:

$$\begin{aligned} \frac{dp(x)}{dt} &= -\frac{d(f(x, t)p(x))}{dx} + \frac{1}{2} \frac{d^2(g^2(x, t)p(x))}{dx^2}, \\ &= -\frac{d(f(x, t)p(x))}{dx} + \left[\frac{1 + \gamma^2(t)}{2} - \frac{\gamma(t)^2}{2} \right] \frac{d^2(g^2(x, t)p(x))}{dx^2} \\ &= -\frac{d}{dx} \left[f(x, t)p(x) - \frac{1 + \gamma^2(t)}{2} \left(\frac{p(x)dg^2(x, t)}{dx} \right. \right. \\ &\quad \left. \left. + \frac{g^2(x, t)dp(x)}{dx} \right) \right] - \frac{1}{2} \frac{d^2([\gamma(t)g(x, t)]^2 p(x))}{dx^2}. \end{aligned}$$

For the diffusion process, since $g(t)$ is independent of \mathbf{X} , we have

$$\begin{aligned} \frac{dp(x)}{dt} &= -\frac{d}{dx} \left[\left(f(x, t) - \frac{1 + \gamma^2(t)}{2} \frac{g^2(x, t)d\log p(x)}{dx} \right) p(x) \right] \\ &\quad - \frac{1}{2} \frac{d^2([\gamma(t)g(x, t)]^2 p(x))}{dx^2}. \end{aligned}$$

Considering for the reverse-time SDE with timestamp of \hat{t} , $d\hat{t} = -dt$, we then have

$$\begin{aligned} \frac{dp(x)}{d\hat{t}} &= -\frac{d}{dx} - \left[\left(f(x, t) - \frac{1 + \gamma^2(t)}{2} \frac{g^2(x, t)d\log p(x)}{dx} \right) p(x) \right] \\ &\quad + \frac{1}{2} \frac{d^2([\gamma(t)g(x, t)]^2 p(x))}{dx^2}. \end{aligned}$$

It actually corresponds to Kolmogorov's forward equation with the following differential equations:

$$\begin{aligned} d\mathbf{X} &= \hat{f}(\mathbf{X}, t)d\hat{t} + g(\hat{t})d\hat{\omega}, \\ \hat{f}(\mathbf{X}, t) &= - \left[f(x, t) - \frac{1 + \gamma^2(t)}{2} \frac{g^2(x, t)d\log p(x)}{dx} \right], \\ g(\hat{t}) &= \gamma(t)g(x, t). \end{aligned}$$

By substituting $d\hat{t} = -dt$ into above equation, we have

$$d\mathbf{X} = \left[f(x, t) - \frac{1 + \gamma^2(t)}{2} g^2(x, t) \nabla_x \log p(x) \right] dt + \gamma(t) g(x, t) d\hat{\omega},$$

which is exactly the Modulated-SDE as we mentioned. Note that the same SDE formulation has been introduced in [3], [4]. However, our proof follows [1] that is more straightforward and complete.

B. Integral Solver of Modulated-SDE

Here we give the calculation of the integral solver for Modulated-SDE. To make such a semi-linear property as [5], we introduce the surrogate function $\mathcal{F}(\mathbf{X}_t, \alpha_t) = \frac{\mathbf{X}_t}{\alpha_t}$. Furthermore, by substituting $f(t) = \frac{d \log \alpha_t}{dt}$ and $g^2(t) = \frac{d\sigma_t^2}{dt} - 2 \frac{d \log \alpha_t}{dt} \sigma_t^2$ from [6], we have

$$\begin{aligned} d\mathcal{F} &= \frac{d^{(\gamma)} \mathbf{X}_t}{\alpha_t} - \frac{\mathbf{X}_t d\alpha_t}{\alpha_t^2} \\ &= \frac{1 + \gamma^2(t)}{2\alpha_t \sigma_t} g^2(t) \epsilon_\theta dt + \gamma(t) g(t) d\hat{\omega} \end{aligned}$$

We take the first-order integral solver as an example. By making integral from both sides, we have

$$\begin{aligned} \mathbf{X}_{t-\Delta t} &= \frac{\alpha_{t-\Delta t}}{\alpha_t} \mathbf{X}_t - [1 + \gamma^2(t)] \epsilon_\theta \left(\frac{\alpha_{t-\Delta t}}{\alpha_t} \sigma_t - \sigma_{t-\Delta t} \right) \\ &\quad - \gamma(t) \epsilon \sqrt{\int_{t-\Delta t}^t (\sigma_t d\sigma_t - \frac{\sigma_t^2}{\alpha_t} d\alpha_t)}. \end{aligned}$$

To derive the closed-form solution, we consider the specific VP and VE diffusion models. For the VP diffusion model ($\alpha_t^2 + \sigma_t^2 = 1$), we have

$$\begin{aligned} \mathbf{X}_{t-\Delta t} &= \frac{\alpha_{t-\Delta t}}{\alpha_t} \mathbf{X}_t - [1 + \gamma^2(t)] \epsilon_\theta \left(\frac{\alpha_{t-\Delta t}}{\alpha_t} \sigma_t - \sigma_{t-\Delta t} \right) \\ &\quad - \gamma(t) \epsilon \alpha_{t-\Delta t} \sqrt{\log \frac{\alpha_{t-\Delta t}}{\alpha_t}}. \end{aligned}$$

While, for the VE diffusion model, we have

$$\begin{aligned} \mathbf{X}_{t-\Delta t} &= \frac{\alpha_{t-\Delta t}}{\alpha_t} \mathbf{X}_t - [1 + \gamma^2(t)] \epsilon_\theta \left(\frac{\alpha_{t-\Delta t}}{\alpha_t} \sigma_t - \sigma_{t-\Delta t} \right) \\ &\quad - \gamma(t) \epsilon \alpha_{t-\Delta t} \sqrt{\alpha_{t-\Delta t}^2 - \alpha_t^2}. \end{aligned}$$

III. PROBABILISTIC FLOW OF RECTIFIED FLOW

In this section, we analyze the probabilistic flow of FLUX [7] to prove that ① the integral formulation of Eq. (13) corresponds to the stochastic formulation of Eq. (12); and ② the ODE in Eq. (6) and the SDE formulation in Eq. (12) in our reinforcement alignment evolve on the same probabilistic flow. Specifically, rectified flow is designed to directly learn the following velocity as

$$dx_t = (x_0 - x_T) dt. \quad (\text{S1})$$

The deterministic formulation of rectified flow is written as

$$x_{t-\Delta t} = x_t - \Delta_t \frac{dx_t}{dt}. \quad (\text{S2})$$

The stochastic formulation of rectified flow is expressed as

$$x_{t-\Delta t} = \frac{[x_t - \alpha_t \Delta_t \frac{dx_t}{dt} - \beta_k \epsilon]}{(1 + \alpha_t \Delta_t - t) + \sqrt{(t - \alpha_t \Delta_t)^2 + \beta_k^2}}, \quad (\text{S3})$$

where α_t is a scalar ($\alpha_t > 1$), and β_k is formulated as

$$\beta_k = \sqrt{\frac{(t - \Delta_t)^2 [1 - (t - \alpha \Delta_t)]^2}{[1 - (t - \Delta_t)]^2} - (t - \alpha \Delta_t)^2}. \quad (\text{S4})$$

Then, we will illustrate that the aforementioned deterministic and stochastic formulations, i.e., Eq. (S2) and Eq. (S3), correspond to the same probabilistic flow. For the probabilistic flow of Eq. (S2), we can derive its formulation by substituting Eq. (S3) into Kolmogorov's forward equation as

$$\begin{aligned} \frac{dp(x)}{dt} &= -\frac{d(f(x, t)p(x))}{dx} + \frac{1}{2} \frac{d^2(g^2(x, t)p(x))}{dx^2}, \\ &= -\frac{d((x_0 - x_T)p(x))}{dx}. \end{aligned} \quad (\text{S5})$$

To derive the probabilistic flow of the stochastic equation, we first substitute Eq. (S4) into the denominator expression of Eq. (S3), obtaining

$$\begin{aligned} &(1 + \alpha_t \Delta_t - t) + \sqrt{(t - \alpha_t \Delta_t)^2 + \beta_k^2} \\ &= (1 - (t - \alpha_t \Delta_t)) + \frac{(t - \Delta_t) [1 - (t - \alpha \Delta_t)]}{[1 - (t - \Delta_t)]} \\ &= \frac{1 - (t - \alpha \Delta_t)}{1 - (t - \Delta_t)}. \end{aligned}$$

Moreover, we also have

$$\beta_k \stackrel{\Delta_t \rightarrow dt}{\approx} \sqrt{2(\alpha_t - 1)} \sqrt{dt}.$$

Then, we can substitute the aforementioned two results accompanied with $x_t = (1 - t)x_0 + tx_T$ together into Eq. (S3), producing

$$\begin{aligned} x_{t-\Delta t} &= \frac{[1 - (t - \Delta_t)]}{[1 - (t - \alpha \Delta_t)]} [x_t - \alpha_t \Delta_t \frac{dx_t}{dt} - \sqrt{2t \alpha_t} \epsilon], \\ &\quad \frac{[1 - (t - \alpha dt)]}{[1 - (t - dt)]} (x_{t-\Delta t} - x_t) \\ &= \frac{(1 - \alpha_t) dt}{1 - (t - dt)} x_t + \alpha_t (x_0 - x_T) dt + \sqrt{2t \alpha_t} d\omega, \\ &- dx = \frac{(1 - \alpha_t) dt}{1 - t} ((1 - t)x_0 + tx_T) \\ &\quad + \alpha_t (x_0 - x_T) dt + \sqrt{2t \alpha_t} d\omega, \end{aligned}$$

$$\textcircled{1} \quad dx = x_0 dt + \frac{t - \alpha_t}{1 - t} x_T dt + \sqrt{2(\alpha_t - 1)} d\omega. \quad (\text{S6})$$

The corresponding Kolmogorov's forward equation can be written as

$$\begin{aligned} \frac{dp(x)}{dt} &= -\frac{d(f(x, t)p(x))}{dx} + \frac{1}{2} \frac{d^2(g^2(x, t)p(x))}{dx^2}, \\ &= -\frac{d \left(\left(x_0 dt + \frac{t - \alpha_t}{1 - t} x_T dt \right) p(x) \right)}{dx} + \frac{(\alpha_t - 1) \frac{d \log p(x)}{dx} p(x)}{dx}. \end{aligned}$$

Since $\frac{d\log p(x)}{dx} = \frac{x_T}{1-t}$, we can conclude the probabilistic flow of Eq. (S3) is

$$\textcircled{2} \quad \frac{dp(x)}{dt} = -\frac{d((x_0 - x_T)p(x))}{dx},$$

which is the same as Eq. (S2). This indicates that the stochastic process described by Eq. (S6) and the deterministic process in Eq. (S1) represent the same probabilistic flow. Consequently, the corresponding integral formulations in Eqs. (S2) and (S3) also describe an identical probabilistic transition process.

IV. TRAJECTORY DISTILLATION COST

A. Calculation of Distillation Cost

In this section, we illustrate the detailed steps for the calculation of the distillation cost. We define the distillation cost as

$$\mathcal{C} = \sum_{i=k}^0 \left\| \check{\epsilon} \left(\frac{\mathbf{X}_i^{i-1}}{t_i^{i-1}} \middle| \frac{d\mathbf{X}_\epsilon}{dt} \right) - \epsilon_\theta(\mathbf{X}_{t_i}, t_i) \right\|_2. \quad (\text{S7})$$

We then start by calculating $\frac{d\mathbf{X}}{d\alpha_t}$ via the DPM-Solver as,

$$\frac{d\mathbf{X}}{d\alpha_t} = \frac{\mathbf{X}_t}{\alpha_t} - \frac{(\sigma_{t-\Delta t} - \frac{\alpha_{t-\Delta t}}{\alpha_t} \sigma_t) \epsilon_\theta}{\alpha_t - \alpha_{t-\Delta t}},$$

Subsequently, we can obtain

$$\check{\epsilon} = \left[\frac{\mathbf{X}_t}{\alpha_t} - \frac{\mathbf{X}_i^{i-1}}{\alpha_i^{i-1}} \right] \frac{\alpha_t - \alpha_{t-\Delta t}}{\sigma_{t-\Delta t} - \frac{\alpha_{t-\Delta t}}{\alpha_t} \sigma_t}.$$

For the VE diffusion model, the gradient is given by

$$\frac{d\mathbf{X}}{d\sigma_t} = -\epsilon_\theta.$$

This leads to the inverted noise

$$\check{\epsilon} = -\frac{\mathbf{X}_i^{i-1}}{\alpha_i^{i-1}}.$$

Finally, the \mathcal{C} can be derived by calculating the L2 Norm of $\check{\epsilon} - \epsilon_\theta$.

B. Proof of Existence

In this section, we first demonstrate the existence of a low-cost distillation strategy. For an arbitrary continuous trajectory and $k \geq 2$, there always exists a distillation strategy with a lower cost than straight flow-based distillation, such as rectified flow or consistency models. However, for $k = 1$, the cost remains the same as that of straight flow-based distillation. Denote by \mathbf{X}_T and \mathbf{X}_0 the clean image and initialized noise, where T and 0 are the corresponding timestamps, and $T_1 \in (0, T)$ a mid timestamp. Then, the distillation cost of the straight flow can be formulated as

$$\begin{aligned} & \left\| \frac{d\mathbf{X}}{dt_0} - \frac{\mathbf{X}_T - \mathbf{X}_0}{T} \right\|_2^2 = \left\| \frac{d\mathbf{X}}{dt_0} - \frac{\mathbf{X}_T - \mathbf{X}_0}{T} \right\|_2^2 \\ &= \|\mathbf{A} + \mathbf{B}\|_2^2, \\ & \mathbf{A} = \frac{T_1 \frac{d\mathbf{X}}{dt_0} - \int_0^{T_1} \frac{d\mathbf{X}}{dt} dt}{T} + \frac{(T - T_1) \frac{d\mathbf{X}}{dt_1} - \int_{T_1}^T \frac{d\mathbf{X}}{dt} dt}{T}, \\ & \mathbf{B} = \frac{(T - T_1)(\frac{d\mathbf{X}}{dt_0} - \frac{d\mathbf{X}}{dt_1})}{T}. \end{aligned}$$

Here, we utilize T_1 to divide $[0, T]$ into 2 segments. Considering a single variable x , we have

$$\begin{aligned} \mathbf{a} &= \frac{T_1 \frac{d\mathbf{x}}{dt_0} - \int_0^{T_1} \frac{d\mathbf{x}}{dt} dt}{T} + \frac{(T - T_1) \frac{d\mathbf{x}}{dt_1} - \int_{T_1}^T \frac{d\mathbf{x}}{dt} dt}{T}, \\ &\stackrel{\textcircled{1}}{=} \frac{T_1}{T} \frac{dx}{dt_0} + \frac{T - T_1}{T} \frac{dx}{dt_1} - \frac{dx}{dt_i} \\ \mathbf{b} &= \frac{(T - T_1)(\frac{dx}{dt_0} - \frac{dx}{dt_1})}{T}, \end{aligned}$$

where $\textcircled{1}$ is based on the mean value theorem for integral. If $t_1 = t_i$, we then have

$$\mathbf{a} = \frac{T_1}{T} \left(\frac{dx}{dt_0} - \frac{dx}{dt_i} \right).$$

Thus, we then have $|\mathbf{a} + \mathbf{b}| = \left| \frac{dx}{dt_0} - \frac{dx}{dt_i} \right| \geq \frac{T_1}{T} \left| \frac{dx}{dt_0} - \frac{dx}{dt_i} \right| = |\mathbf{a}|$. There will always be a low-cost distillation point for $k = 2$ than $k = 1$ (rectified flow/ consistency model). We can then easily derive similar results for higher k with iterative application of the aforementioned process in sub-intervals.

V. SYNTHESIZING NOISE LATENT HELPS IR DIFFUSION

Assume the noise-prediction neural $\epsilon_\theta(\cdot)$ has Lipschitz continuity, i.e., $\|\epsilon_\theta(\mathbf{X}_0) - \epsilon_\theta(\mathbf{X}_1)\|_2 \leq k \|\mathbf{X}_0 - \mathbf{X}_1\|_2$. Then, we take a one-step distillation model for example

$$\begin{aligned} \mathbf{X}_{T \rightarrow 0} &= \frac{\alpha_0}{\alpha_T} \mathbf{X}_T + \alpha_0 e^{-\lambda} \Big|_{\lambda_T}^{\lambda_0} \hat{\epsilon}_\theta(\hat{\mathbf{X}}_T, T), \\ \mathbf{X}_{T-\delta \rightarrow 0} &= \frac{\alpha_0}{\alpha_{T-\delta}} \mathbf{X}_{T-\delta} + \alpha_0 e^{-\lambda} \Big|_{\lambda_{T-\delta}}^{\lambda_0} \hat{\epsilon}_\theta(\hat{\mathbf{X}}_{T-\delta}, T - \delta), \end{aligned}$$

We can then get the optimal noise estimation via making $\mathbf{X}_{T \rightarrow 0}$ $\mathbf{X}_{T-\delta \rightarrow 0}$ to be the ground-truth value \mathbf{X}_0 . Then the optimal noise can be formulated as

$$\epsilon_{T-\delta \rightarrow 0} = \frac{\frac{\mathbf{X}}{\sigma_0} - SNR_0 \mathbf{Y} - \frac{SNR_0}{SNR_{T-\delta}} \epsilon}{1 - \frac{SNR_0}{SNR_{T-\delta}}},$$

$$\epsilon_{T \rightarrow 0} = \frac{\frac{\mathbf{X}}{\sigma_0} - \frac{SNR_0}{SNR_T} \epsilon}{1 - \frac{SNR_0}{SNR_T}},$$

where SNR indicates the signal to noise ratio, i.e., $SNR_0 = \frac{\alpha_0}{\sigma_0}$. We assume that the potential error of a neural network \mathcal{E} is positively correlated with the shift between the target and input, i.e., $\mathcal{E} = k \|\mathbf{X}_{in} - \mathbf{X}_{out}\|_2$, where $k > 0$. Thus, we

can easily measure the magnitude of error by calculating the following ratio:

$$\begin{aligned}
\frac{\mathcal{E}_{T-\delta}}{\mathcal{E}_T} &= \mathbb{E}_{\epsilon \sim \mathcal{N}(\mathbf{0}, \mathbf{I})} \frac{\|\epsilon_{T-\delta \rightarrow 0} - \epsilon\|_2}{\|\epsilon_{T \rightarrow 0} - \epsilon\|_2} \\
&= \mathbb{E}_{\epsilon \sim \mathcal{N}(\mathbf{0}, \mathbf{I})} \frac{\left\| \frac{\mathbf{X}}{\sigma_0} - SNR_0 \mathbf{Y} - \epsilon \right\|_2}{\left\| \frac{\mathbf{X}}{1 - \frac{SNR_0}{SNR_{T-\delta}}} - \epsilon \right\|_2} \\
&\stackrel{\textcircled{1}}{\approx} \frac{SNR_{T-\delta}}{SNR_T} \frac{\mathbb{E}_{\epsilon \sim \mathcal{N}(\mathbf{0}, \mathbf{I})} \left\| \frac{\mathbf{X}}{\sigma_0} - SNR_0 \mathbf{Y} - \epsilon \right\|_2}{\mathbb{E}_{\epsilon \sim \mathcal{N}(\mathbf{0}, \mathbf{I})} \left\| \frac{\mathbf{X}}{\sigma_0} - \epsilon \right\|_2} \\
&= \frac{SNR_{T-\delta}}{SNR_T} \frac{\sqrt{\left\| \frac{\mathbf{X}}{\sigma_0} - SNR_0 \mathbf{Y} \right\|_2^2 + dim(\epsilon)}}{\sqrt{\left\| \frac{\mathbf{X}}{\sigma_0} \right\|_2^2 + dim(\epsilon)}}, \\
&\stackrel{\textcircled{2}}{\approx} \frac{SNR_{T-\delta}}{SNR_T} \frac{\left\| \frac{\mathbf{X}}{\sigma_0} - SNR_0 \mathbf{Y} \right\|_2}{\left\| \frac{\mathbf{X}}{\sigma_0} \right\|_2} \stackrel{\textcircled{3}}{\approx} \frac{SNR_{T-\delta}}{SNR_T} \frac{\|\mathbf{X} - \mathbf{Y}\|_2}{\|\mathbf{X}\|_2}
\end{aligned}$$

where $dim(\cdot)$ indicates the number of elements in the input tensor. ① for $\frac{SNR_0}{SNR_{T-\delta}} \gg 1$, we have $\frac{SNR_0}{SNR_T} \gg 1$. ② for $\sigma_0 \rightarrow 0$ thus $\left\| \frac{\mathbf{X}}{\sigma_0} \right\|_2^2 \gg dim(\epsilon)$ and ③ for $\alpha_0 \rightarrow 1$. Meanwhile, for image restoration tasks, we usually have $\|\mathbf{X} - \mathbf{Y}\|_2 \leq k_1 \|\mathbf{X}\|_2$, where $0 \leq k_1 \leq 1$. Thus, we have $\frac{\mathcal{E}_{T-\delta}}{\mathcal{E}_T} \leq k_1$. If we utilize a small network to adaptively learn an initialization value to replace \mathbf{Y} , we can further reduce k_1 .

VI. MORE VISUAL RESULTS

In this section, we show additional visual results. Specifically, Figs. 1, 2, and 3 illustrate visual comparisons for underwater image enhancement, low-light enhancement, and deraining, respectively, under the task-specific setting. Fig. 4 showcases the experimental results for unified image restoration. Finally, Fig. 5 shows the visual comparison of ablation studies.

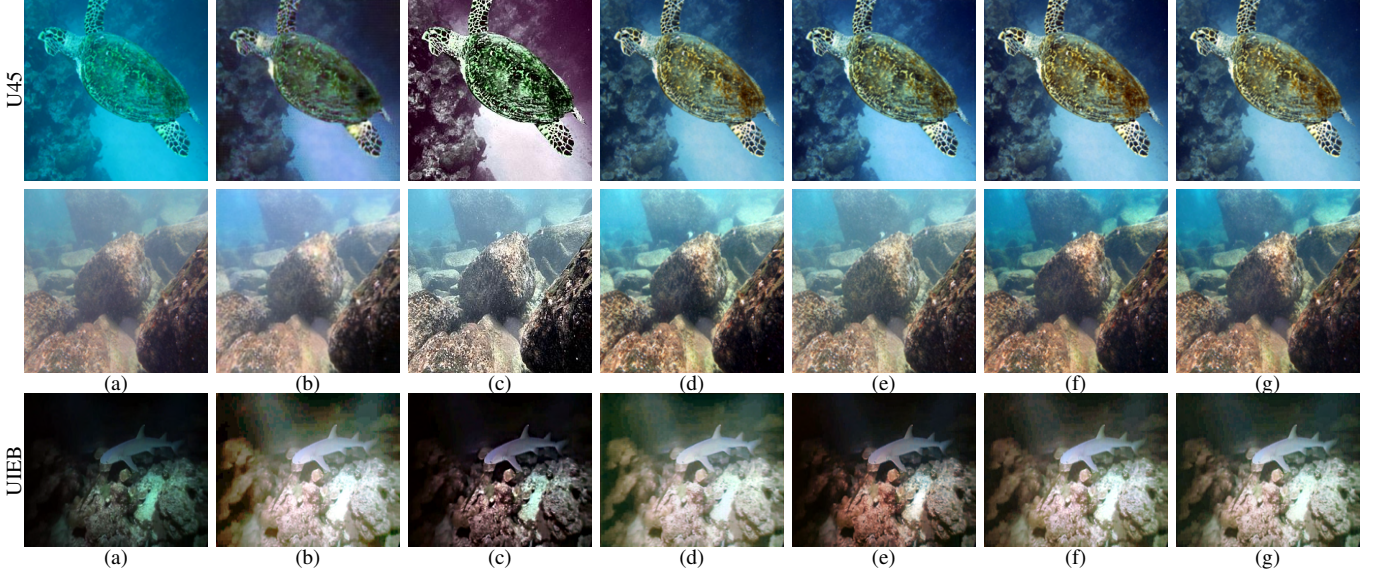


Fig. 1. Visual comparison of underwater image enhancement on U45 [8] and UIEB [9] datasets. U45 (**top**): (a) low-quality input, (b) CycleGAN [10], (c) MLLE [11], (d) HCLR [12], (e) SemiUIR [13], (f) Ours($NFE = 1$) and (g) Ours($NFE = 10$). UIEB (**bottom**): except (b) reference image, the remaining columns are the same as those of U45.

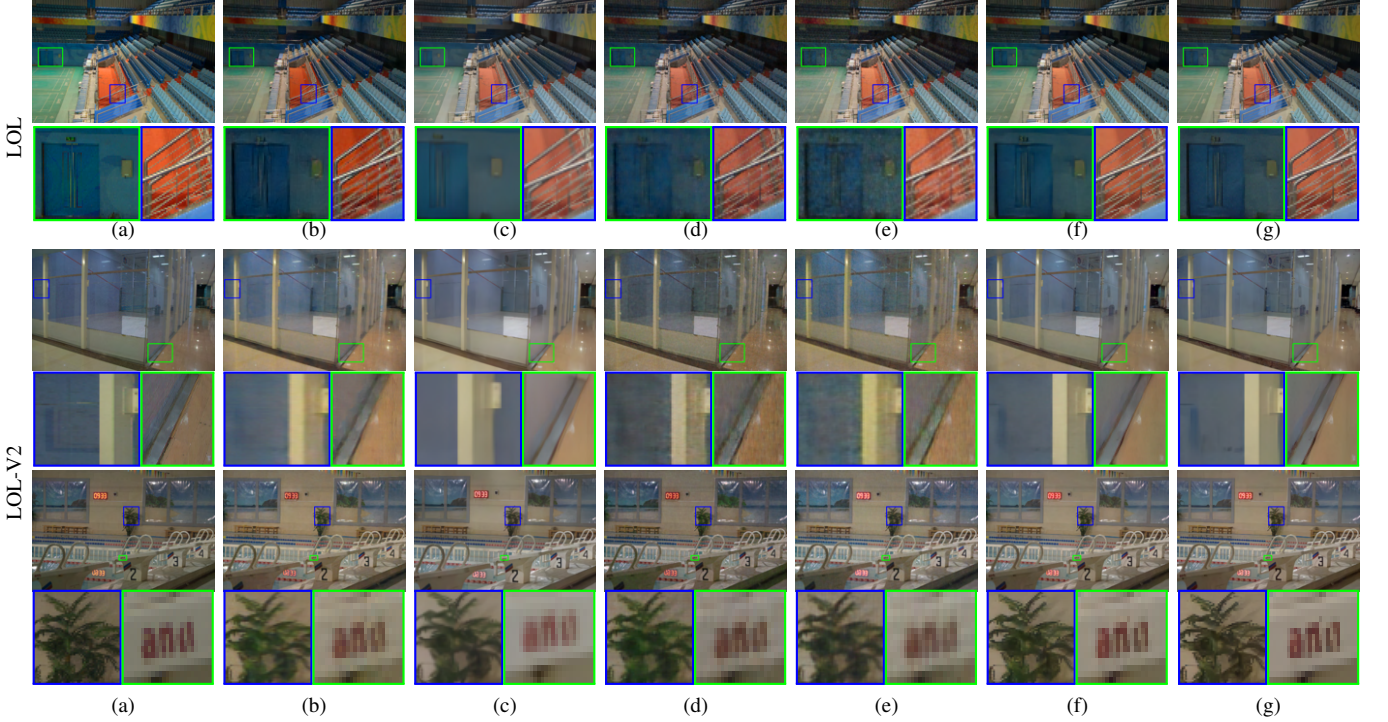


Fig. 2. Visual comparison of low-light enhancement on LOL and LOLV2 datasets. LOL (**top**): (a) reference images, (b) CID [14], (c) LLFlow [15], (d) RetinexFormer [16], (e) LLFormer [17], (f) Ours ($NFE = 1$), (g) Ours ($NFE = 10$). LOLV2 (**bottom**): except (b) SNR-Aware [18], the remaining columns are the same as those of LOL. Below each figure, we also visualize zoom-in regions marked by the blue and green boxes.



Fig. 3. Visual comparison on the tasks of raindrop removal and image deraining. Raindrop removal (**top**): (a) low-quality input, (b) reference samples, (c) IDT [19], (d) GridFormer [20], (e) RainDropDiff [21], (f) Ours ($NFE = 1$), (g) Ours ($NFE = 10$). Deraining (**bottom**): (a) low-quality input, (b) reference samples, (c) GridFormer [20], (d) WeatherDiff64 [21], (e) WeatherDiff128 [21], (f) Ours ($NFE = 1$), (g) Ours ($NFE = 10$).



Fig. 4. Additional visual comparison of unified image restoration. In the super-resolution task, (a)-(f) indicates the input low-quality measurement, reference image, PASD [22], SeeSR [23], and FLUX-IR(Ours), respectively. We annotated evaluation metrics of corresponding images by PSNR ↑, NIQE ↓, and MUSIQ ↑, respectively.

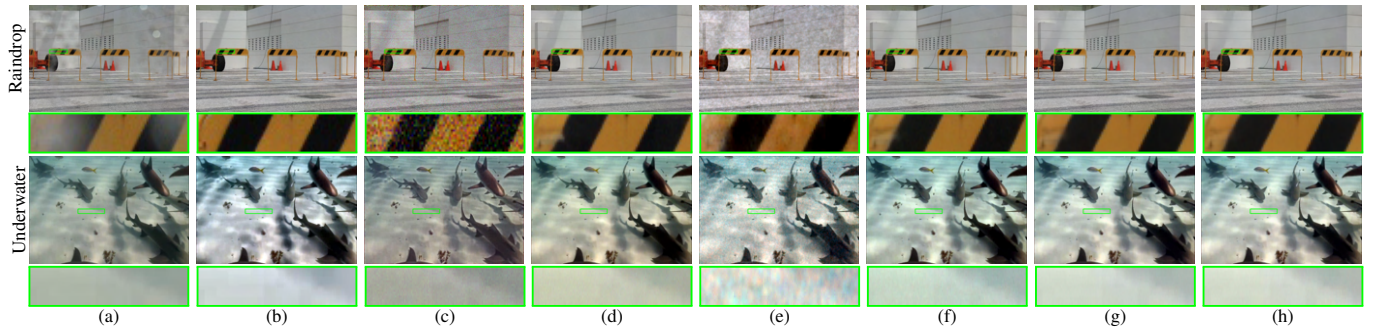


Fig. 5. Visual demonstration of ablation studies. (a) low-quality image, (b) reference image, (c) pretrained model ($NFE = 1$, Table XI-1), (d) pretrained model ($NFE = 10$, Table XI-1), (e) RL ($NFE = 1$, Table XI-2), (f) RL w/ DISTILL ($NFE = 1$, Table XI-3), (g) (f) w/ latent INTER ($NFE = 1$, Table XI-4), (h) (g) w/ NGS ($NFE = 1$, Table XI-5)

REFERENCES

- [1] Y. Song, J. Sohl-Dickstein, D. P. Kingma, A. Kumar, S. Ermon, and B. Poole, "Score-based generative modeling through stochastic differential equations," in *Proc. ICLR*, 2021, pp. 1–12.
- [2] B. Øksendal and B. Øksendal, *Stochastic differential equations*. Springer, 2003.
- [3] Q. Zhang and Y. Chen, "Diffusion normalizing flow," in *Proc. NeurIPS*, vol. 34, 2021, pp. 16 280–16 291.
- [4] ———, "Fast sampling of diffusion models with exponential integrator," *arXiv preprint arXiv:2204.13902*, 2022.
- [5] C. Lu, Y. Zhou, F. Bao, J. Chen, C. Li, and J. Zhu, "Dpm-solver: A fast odes solver for diffusion probabilistic model sampling in around 10 steps," in *Proc. NeurIPS*, vol. 35, 2022, pp. 5775–5787.
- [6] D. Kingma, T. Salimans, B. Poole, and J. Ho, "Variational diffusion models," in *Proc. NeurIPS*, vol. 34, 2021, pp. 21 696–21 707.
- [7] B. Andreas, S. Axel, L. Dominik, P. Dustin, B. Frederic, S. Harry, M. Jonas, L. Kyle, E. Patrick, R. Robin, K. Sumith, D. Tim, L. Yam, and E. Zion, "Flux," 2024. [Online]. Available: <https://blackforestlabs.ai/>
- [8] C. Ancuti, C. O. Ancuti, T. Haber, and P. Bekaert, "Enhancing underwater images and videos by fusion," in *Proc. IEEE CVPR*, 2012, pp. 81–88.
- [9] C. Li, C. Guo, W. Ren, R. Cong, J. Hou, S. Kwong, and D. Tao, "An underwater image enhancement benchmark dataset and beyond," *IEEE Transactions on Image Processing*, vol. 29, pp. 4376–4389, 2019.
- [10] J.-Y. Zhu, T. Park, P. Isola, and A. A. Efros, "Unpaired image-to-image translation using cycle-consistent adversarial networks," in *Proc. IEEE ICCV*, 2017, pp. 2223–2232.
- [11] W. Zhang, P. Zhuang, H.-H. Sun, G. Li, S. Kwong, and C. Li, "Underwater image enhancement via minimal color loss and locally adaptive contrast enhancement," *IEEE Transactions on Image Processing*, vol. 31, pp. 3997–4010, 2022.
- [12] J. Zhou, J. Sun, C. Li, Q. Jiang, M. Zhou, K.-M. Lam, W. Zhang, and X. Fu, "Hclr-net: Hybrid contrastive learning regularization with locally randomized perturbation for underwater image enhancement," *International Journal of Computer Vision*, vol. 132, no. 10, pp. 4132–4156, 2024.
- [13] S. Huang, K. Wang, H. Liu, J. Chen, and Y. Li, "Contrastive semi-supervised learning for underwater image restoration via reliable bank," in *Proc. IEEE CVPR*, 2023, pp. 18 145–18 155.
- [14] Y. Feng, C. Zhang, P. Wang, P. Wu, Q. Yan, and Y. Zhang, "You only need one color space: An efficient network for low-light image enhancement," *arXiv preprint arXiv:2402.05809*, 2024.
- [15] Y. Wang, R. Wan, W. Yang, H. Li, L.-P. Chau, and A. Kot, "Low-light image enhancement with normalizing flow," in *Proc. AAAI*, vol. 36, no. 3, 2022, pp. 2604–2612.
- [16] Y. Cai, H. Bian, J. Lin, H. Wang, R. Timofte, and Y. Zhang, "Retinex-former: One-stage retinex-based transformer for low-light image enhancement," in *Proc. IEEE ICCV*, 2023, pp. 12 504–12 513.
- [17] T. Wang, K. Zhang, T. Shen, W. Luo, B. Stenger, and T. Lu, "Ultra-high-definition low-light image enhancement: A benchmark and transformer-based method," in *Proc. AAAI*, vol. 37, no. 3, 2023, pp. 2654–2662.
- [18] X. Xu, R. Wang, C.-W. Fu, and J. Jia, "Snr-aware low-light image enhancement," in *Proc. IEEE CVPR*, 2022, pp. 17 714–17 724.
- [19] J. Xiao, X. Fu, A. Liu, F. Wu, and Z.-J. Zha, "Image de-raining transformer," *IEEE Transactions on Pattern Analysis and Machine Intelligence*, vol. 45, no. 11, pp. 12 978–12 995, 2022.
- [20] T. Wang, K. Zhang, Z. Shao, W. Luo, B. Stenger, T. Lu, T.-K. Kim, W. Liu, and H. Li, "Gridformer: Residual dense transformer with grid structure for image restoration in adverse weather conditions," *International Journal of Computer Vision*, pp. 1–23, 2024.
- [21] O. Özdenizci and R. Legenstein, "Restoring vision in adverse weather conditions with patch-based denoising diffusion models," *IEEE Transactions on Pattern Analysis and Machine Intelligence*, vol. 45, no. 8, pp. 10 346–10 357, 2023.
- [22] T. Yang, R. Wu, P. Ren, X. Xie, and L. Zhang, "Pixel-aware stable diffusion for realistic image super-resolution and personalized stylization," in *Proc. ECCV*, 2024, pp. 74–91.
- [23] R. Wu, T. Yang, L. Sun, Z. Zhang, S. Li, and L. Zhang, "Seesr: Towards semantics-aware real-world image super-resolution," in *Proc. IEEE CVPR*, 2024, pp. 25 456–25 467.